

# PROBING THE LOW-REDSHIFT STAR FORMATION RATE AS A FUNCTION OF METALLICITY THROUGH THE LOCAL ENVIRONMENTS OF TYPE II SUPERNOVAE

R. STOLL<sup>1</sup>, J.L. PRIETO<sup>2,3</sup>, K.Z. STANEK<sup>1,4</sup>, R.W. POGGE<sup>1,4</sup>

*Draft version June 24, 2013*

## ABSTRACT

Type II SNe can be used as a star formation tracer to probe the metallicity distribution of global low-redshift star formation. We present oxygen and iron abundance distributions of type II supernova progenitor regions that avoid many previous sources of bias. Because iron abundance, rather than oxygen abundance, is of key importance for the late stage evolution of the massive stars that are the progenitors of core-collapse supernovae, and because iron enrichment lags oxygen enrichment, we find a general conversion from oxygen abundance to iron abundance. The distributions we present here are the best yet observational standard of comparison for evaluating how different classes of supernovae depend on progenitor metallicity. We spectroscopically measure the gas-phase oxygen abundance near a representative subsample of the hosts of type II supernovae from the first-year Palomar Transient Factory (PTF) supernova search, using a combination of SDSS spectra near the supernova location (9 hosts) and new longslit spectroscopy (25 hosts). The median metallicity of these 34 hosts at or near the supernova location is  $12+\log(\text{O}/\text{H}) = 8.65$ , with a median error of 0.09. The median host galaxy stellar mass from fits to SDSS photometry is  $10^{9.9} M_{\odot}$ . They do not show a systematic offset in metallicity or mass from a redshift-matched sample of the MPA/JHU value-added catalog. In contrast to previous supernova host metallicity studies, this sample is drawn from a single survey. It is also drawn from an areal rather than a targeted survey, so supernovae in the lowest-mass galaxies are not systematically excluded. Indeed, the PTF supernova search has a slight bias towards following up transients in low mass galaxies. The progenitor region metallicity distribution we find is statistically indistinguishable from the metallicity distribution of type II supernova hosts found by targeted surveys and by samples from multiple surveys with different selection functions. Using the relationship between iron and oxygen abundances found for Milky Way disk, bulge, and halo stars, we translate our distribution of type II SN environments as a function of oxygen abundance into an estimate of the iron abundance, since iron varies more steeply than oxygen. We find that though this sample spans only 0.65 dex in oxygen abundance, the gap between the iron and oxygen abundance is 50% wider at the low-metallicity end of our sample than at the high-metallicity end.

*Keywords:* (stars:) supernovae: general; galaxies: abundances; galaxies: dwarf

## 1. INTRODUCTION

The question of how certain rare classes of supernovae (SNe) depend on progenitor metallicity has been limited by the lack of an unbiased standard of comparison. It is incorrect to use the metallicity distribution of galaxies for this because core-collapse supernovae (CCSNe) trace star formation rather than stellar mass. Existing supernova host galaxy metallicity distributions are selected to compare matched samples and use supernova surveys that do not search in the faintest hosts, and are not likely to be suitable as a standard of comparison for rare events that appear to be more common in low-mass galaxies. We address this by measuring a metallicity distribution of type II supernova progenitor regions from a single source survey that is areal rather than targeted.

The observational properties of CCSNe span a broad range of spectral types, luminosities, apparent kinetic energies, and other properties. Interpreting this diversity remains a fundamental theoretical and observational challenge, particularly as to how differences in the stel-

lar progenitors of the SNe are related to the explosions. For example, the relative fractions of hydrogen-rich type II SNe and hydrogen-poor type Ib/c SNe can be predicted as a function of metallicity based on models for mass-loss from the progenitor stars (Eldridge et al. 2008; Georgy et al. 2009, 2012). Standard mass loss models for massive stars are based on line-driven winds (e.g. Kudritzki & Puls 2000); the efficiency of these winds depends on metallicity because metals, particularly iron, dominate the line opacities driving the winds (Vink & de Koter 2005). Furthermore, the explosion energy of normal type II SNe may depend on the progenitor metallicity (Kasen & Woosley 2009), and certain types of SNe may occur only for low-metallicity progenitor stars (Ober et al. 1983; Heger & Woosley 2002; Langer et al. 2007).

A serendipitous observation of a SN progenitor star prior to explosion is one useful way to characterize the progenitor and determine how the SN properties depend on progenitor properties. Unfortunately, observing or strongly constraining the properties of the progenitor star is only possible for SNe in nearby galaxies, leading to very small samples (e.g. Smartt 2009, and references therein). This limits the utility of this technique for constraining the properties of subclasses of events that are

<sup>1</sup> Department of Astronomy, The Ohio State University

<sup>2</sup> Department of Astrophysical Sciences, Princeton University

<sup>3</sup> Hubble and Carnegie-Princeton Fellow

<sup>4</sup> Center for Cosmology and AstroParticle Physics, The Ohio State University

rare and therefore observed mostly at large distances, such as extremely optically luminous CCSNe.

Observational techniques for addressing this question without pre-explosion data involve estimating the progenitor properties from the environments that remain behind. These techniques range from estimating progenitor age and mass from the degree of correlation with  $H\alpha$  (Anderson & James 2008) and NUV (Anderson et al. 2012) emission, to detailed characterization of resolved stellar populations near supernova explosion sites in nearby galaxies (Badenes et al. 2009; Murphy et al. 2011) to extrapolation of stellar population properties from galaxy photometry and spectroscopic observations (e.g. Kelly et al. 2008; Arcavi et al. 2010; Kelly & Kirshner 2012).

Spectroscopic observations of H II regions near a supernova can be used to estimate the metallicity using strong-line oxygen abundance indicators. There are precision and accuracy limitations to strong-line abundance estimates, but more rigorous abundance measurements using faint auroral lines are too costly (or completely unfeasible) for statistical surveys of SN host metallicities.

The frequency of several classes of CCSN types has been found to vary with host metallicity. Prantzos & Boissier (2003) found that the ratio between type Ib/c and type II SNe increases with increasing host luminosity, and because of the galaxy luminosity/metallicity relationship, they suggested this was probably a metallicity effect. This was confirmed and expanded upon by Prieto et al. (2008) in a subsequent study, which found that hosts of type Ib/c SNe are higher metallicity than hosts of type II and type Ia SNe based on spectroscopically measured metallicity. Stanek et al. (2006) found that type Ic SNe associated with nearby long gamma-ray bursts (GRBs) were in faint, metal-poor galaxies, proposing a progenitor metallicity cutoff above which GRBs do not occur, and Modjaz et al. (2008) found that type Ic SNe that were associated with GRBs were in more metal-poor regions than those that were not. Anderson et al. (2010) found at marginal significance that type Ib and type Ic SNe hosts have slightly higher metallicity than hosts of type II and type Ia SNe. The metallicity local to type Ic SNe without broad lines was found by Modjaz et al. (2011) to be on average higher than near type Ib SNe, regardless of which strong-line metallicity diagnostic was used, consistent with the results of Kelly & Kirshner (2012), though Anderson et al. (2010) and Leloudas et al. (2011) found the difference to not be statistically significant. Kelly & Kirshner (2012) found that although hosts of type Ib and type Ic SNe are higher in metallicity than hosts of type II SNe, hosts of broad-lined type Ic (Ic-BL) SNe are lower in metallicity.

CCSNe which are abnormally optically luminous appear to occur more often in low-mass, low-luminosity galaxies (Neill et al. 2011). Spectroscopic abundance measurements of hosts of five such luminous CCSNe indicate this is likely due to metallicity, as shown by Stoll et al. (2011) (including data from Young et al. 2010; Kozłowski et al. 2010). These abnormally luminous CCSNe are predominantly SNe Ic or IIn. Subsequent spectroscopic measurements of the host of the luminous SN 2008am (Chatzopoulos et al. 2011) and the luminous SN 2010ay (Prieto & Filippenko 2010;

Modjaz et al. 2010; Sanders et al. 2012), and photometric limits on the hosts of the luminous SNe PS1-10awh and PS1-10ky (Chomiuk et al. 2011) reinforce this conclusion.

Many studies (e.g. Neill et al. 2009; Sanders et al. 2012; Stoll et al. 2011; Campisi et al. 2011; Vergani et al. 2011) compare host galaxies of SNe or GRBs to the overall galaxy population, which is a good way to put the host metallicity results in context. It is not, however, a secure way to evaluate whether metallicity is a key parameter governing whether a supernova has a given spectral type or luminosity. Supernovae trace star formation rather than overall stellar mass, and star formation is not evenly distributed among galaxies of a given mass. Recent results (Lara-López et al. 2010; Mannucci et al. 2010) show that the scatter in the galaxy mass-metallicity relationship may be reduced by considering star formation as a third parameter, and that star formation rates (SFRs) are higher in lower metallicity galaxies at a given mass (but see also Yates et al. 2012, which finds that the form of any such relation between mass, metallicity, and star formation rate depends on the strong-line metallicity diagnostic used).

Levesque et al. (2010) and Han et al. (2010) suggested that instead of a metallicity cutoff for GRBs there is a separate luminosity-metallicity relationship for GRB host galaxies offset to lower metallicity than the normal galaxy mass-metallicity relationship of Tremonti et al. (2004). (These results are consistent with a simple metallicity cutoff with the exception of a single high-mass GRB host galaxy that appears to be high metallicity.) No such offset has been observed for type Ia SNe (Neill et al. 2009). This question of an offset in the mass-metallicity relationship has confused many subsequent discussions of a metallicity cutoff.

Mannucci et al. (2011) notes that for galaxies at a given mass, lower metallicity galaxies have higher average star formation rates (Mannucci et al. 2010) and thus core-collapse events, which trace star formation, should have a mass-metallicity distribution shifted to slightly lower metallicity at a given mass. This effect is qualitatively similar enough to the offset proposed by Levesque et al. (2010) and Han et al. (2010) that Mannucci et al. (2011) conclude that GRB hosts do not differ substantially from the typical galaxy population and therefore there is no metallicity dependence to GRB hosts. Kocevski & West (2011) quantifies the expected metallicity shift, and finds that the star-formation-weighted relationship between galaxy mass and metallicity is shifted towards lower metallicity at a given mass, but that this alone cannot explain the observed GRB host distribution, and a metallicity dependence is still required. Many subsequent studies have claimed to disprove any dependence on metallicity for GRBs or luminous SNe by showing that the host galaxy metallicity is consistent with its mass and star formation rate according to the relationship between the three (Lara-López et al. 2010; Mannucci et al. 2010). While this is evidence against a distinct mass-metallicity relationship for the hosts of these SNe, it is not evidence against a *metallicity dependence*.

This shift can also be quantified semi-analytically by convolving the galaxy mass function with the relationship between galaxy mass, metallicity, and star formation

rate to find the overall distribution of star formation as a function of metallicity. Niino (2011) does so by comparing the observed metallicity distribution of GRB hosts to the metallicity distribution of star formation, calculated two different ways; first, calculated observationally from the stellar mass function, the galaxy M-SFR relation, and the galaxy mass-metallicity relation, and second, calculated using the relationship between galaxy mass, metallicity, and SFR defined by Mannucci et al. (2010), and assigning metallicities based on SFR as well as mass. He finds the difference between these two estimates is less than 0.5 dex in oxygen abundance on the KK04 scale. Regardless which method is used, he finds that the GRB host metallicity distribution is incompatible with the metallicity distribution of star formation unless the GRB fraction depends on metallicity. (This is not the primary result of that study, which examines the fact that galaxies do not have one single metallicity, but show an internal spread. Assuming a hypothetical transient phenomenon which has a strict cutoff metallicity above which it cannot occur, Niino (2011) shows that such a spread in internal galaxy metallicities would serve to widen the observed host metallicity distribution of that transient phenomenon.)

Only by comparing the metallicity distribution of a SN variety to the overall metallicity distribution of star formation can one rigorously test for a metallicity dependence. Our metallicity distribution of type II SN hosts can serve as a standard of comparison for evaluating how rare classes of SNe depend on progenitor metallicity.

Essentially all of these previous studies relating metallicity and SN properties draw on SN samples from multiple surveys. A perfectly homogeneous and unbiased SN sample does not currently exist. At present, the Palomar Transient Factory (Rau et al. 2009, PTF) appears to supply the closest approximation to this, in the sense that the SN selection does not exclude the smallest, most vigorously star-forming galaxies. This would not be true, for example, of the Lick Observatory Supernova Search (LOSS) survey (Li et al. 2011), which explicitly targets larger galaxies. In contrast, the PTF biases their followup slightly towards supernovae in low-mass galaxies (I. Arcavi, private communication). In this paper we will focus on the 52 type II SNe found in the first year of PTF operations. Because some subtypes of CCSNe are known to have different distributions in host metallicity, we focus on type II SNe. We have measured metallicities for the environments of a representative subsample of 34 of these type II SNe, and present the resulting metallicity distribution.

This distribution probes the low-redshift star formation rate as a function of metallicity in an independent way from current methods relying on galaxy population statistics. This is an important distribution to characterize because in order to determine whether a massive star outcome has a metallicity dependence, we need to examine its frequency relative to the metallicity distribution of star formation, not to the metallicity distribution of existing stellar mass (the galaxy metallicity distribution). Because the PTF followup is biased slightly towards transients in lower mass host galaxies, we expect the progenitor region metallicity distribution we measure may be slightly more metal-poor than the true overall progenitor distribution of type II SNe. This makes our

distribution a rigorous standard of comparison for a population suspected to be metal-poor; if that population is significantly more metal-poor than the distribution we present here, it is certainly more metal-poor than the overall distribution of type II SNe.

We place the metallicity distribution of type II SNe environments in context by comparing it with previous supernova host studies (Prieto et al. 2008; Anderson et al. 2010; Kelly & Kirshner 2012), with the SDSS DR7 MPA/JHU value-added catalog (Kauffmann et al. 2003; Tremonti et al. 2004; Brinchmann et al. 2004; Salim et al. 2007), and with estimates from galaxy population statistics (Stanek et al. 2006). Noting that iron is more fundamental than oxygen to the evolutionary outcomes of massive stars because iron opacity drives stellar winds, we then translate our oxygen abundance distribution of type II SNe environments into an iron abundance distribution by using the observed relationship between oxygen and iron abundance in Milky Way bulge, disk, and halo stellar abundances.

## 2. SPECTROSCOPIC OBSERVATIONS AND ANALYSIS

We drew our targets from the first-year of the Palomar Transient Factory (PTF) survey (Arcavi et al. 2010), an areal rather than a targeted survey, so supernovae in the lowest-mass galaxies are not excluded by selection. The sample selection for the survey is not yet published, but transients in dwarf hosts are prioritized for spectroscopic followup (I. Arcavi, private communication), so a slight bias towards metal-poor environments is expected. In contrast, a bias towards metal-rich environments would be expected for galaxy-targeted surveys, which miss low-mass galaxies entirely. There are 52 type II SNe in the full first-year PTF CCSN sample, of which we have measured spectroscopic metallicity determinations for a subsample of 34. This subsample is representative of the overall type II sample, as we show in §4.1.

We obtained host galaxy spectra of these SNe using the Ohio State Multi-Object Spectrograph (OSMOS, Martini et al. 2011; Stoll et al. 2010) on the 2.4-m Hiltner telescope, the Wide Field Reimaging CCD Camera (WFCCD) on the 2.5-m du Pont telescope, and the dual imaging spectrograph (DIS) on the 3.5-m Astrophysical Research Consortium telescope. We also use twelve archival spectra from SDSS DR7 (Abazajian et al. 2009; Uomoto et al. 1999; York et al. 2000; Gunn et al. 2006). The properties of the spectroscopic observations are summarized in Table 1. We processed the data using standard techniques in IRAF<sup>5</sup>, individually extracting each spectrum. Relative flux calibration was done with observations of spectrophotometric standard stars taken each night. The PP04N2 metallicity diagnostic is extremely insensitive to reddening because it depends on the flux ratio of two very close lines, so intrinsic extinction corrections were not applied. Images of nine representative type II hosts spanning the observed range of metallicity and galaxy mass are shown in Figure 1. We also measured spectroscopic metallicities for the hosts of three type Ib, two type IIb, three type Ic, and one type Ic-BL

<sup>5</sup> IRAF is distributed by the National Optical Astronomy Observatory, which is operated by the Association of Universities for Research in Astronomy (AURA) under cooperative agreement with the National Science Foundation.

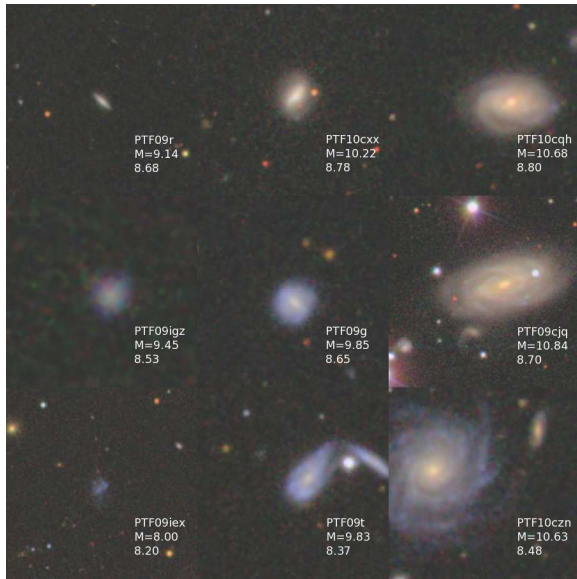


**Figure 1.** Nine type II SN hosts, spanning the metallicity and mass range, arranged so mass increases toward the right and oxygen abundance increases toward the top. Each panel is scaled to a physical size of 50 kpc ( $H_0, \Omega_m, \Omega_\Lambda = 70, 0.3, 0.7$ ) and is centered on the position of the supernova. All images are from SDSS and were taken before the supernovae.

from the first-year PTF sample. These numbers are too small for rigorous statistical comparison, so we exclude these from our analysis of the type II sample, and discuss them further in § 4.5.

The new observations were made either at the supernova position or at a similar galactocentric radius to minimize any biases from metallicity gradients in the host galaxies. We include the angular distance from the host galaxy center to the supernova site in Table 2 for easy comparison to the seeing and to the spectroscopic aperture, listed in Table 1. We include the projected physical distance from the galaxy center to facilitate future comparison to studies that use galactocentric spectra. The SDSS spectra are the only spectra taken at the galaxy center rather than at the galactocentric radius of the supernova. Note that for these SDSS spectra, most SN locations are within the fiber diameter, and only one is more than 2 fiber diameters away. We obtained new spectra for any hosts with existing SDSS spectra more distant than this. Any resulting effect from galactic metallicity gradients on the metallicity distribution should be minimal. Line fluxes of  $H\alpha \lambda 6563$  and  $[N II] \lambda 6584$  are given in Table 2.

For host galaxies with multiple SDSS spectra or with spectra from multiple sources, we fit a metallicity gradient where possible and provide the best fit metallicity at the galactocentric radius of the supernova progenitor; these are labeled as ‘grad’. Line fluxes, observed galactocentric radii, and derived metallicity for these measurements are given in Table 3.

We primarily consider host metallicities determined with the N2 diagnostic of Pettini & Pagel (2004), which we directly measure for each of our targets. This diagnostic depends solely on  $[N II] \lambda 6584 / H\alpha \lambda 6563$ , and is extremely insensitive to reddening, though it has a larger intrinsic scatter than other strong-line diagnostics based

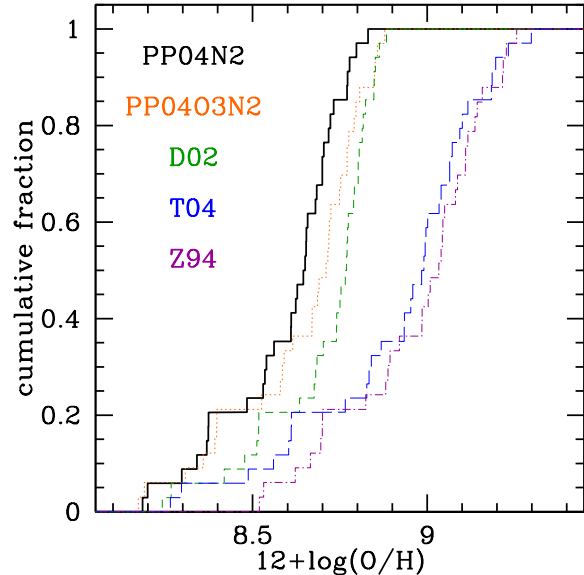


**Figure 2.** Cumulative distribution of local gas-phase oxygen abundances for type II SNe. As type II SNe trace young stellar populations, this traces the metallicity distribution of star formation at low redshift. The solid black distribution uses the N2 diagnostic of Pettini & Pagel (2004, PP04) we adopt as our standard. Subsequent figures only use these measurements. The other distributions show how the result would change for other strong-line metallicity diagnostics, based on the empirical conversions of Kewley & Ellison (2008). The dotted orange curve uses the PP04 O3N2 diagnostic, the short-dashed green curve uses Denicoló et al. (2002), the long-dashed blue curve uses Tremonti et al. (2004), the dot-dashed purple curve uses Zaritsky et al. (1994). We do not show conversions to the scales of Kobulnicky & Kewley (2004), McGaugh (1991), and Kewley & Dopita (2002), which require external branch information.

on the physical conditions of the H II regions. There are a number of techniques that are used to estimate the oxygen abundances of H II regions in star-forming galaxies, and a substantial literature discussing their various merits and drawbacks (e.g. Kewley & Ellison 2008, and references therein). A full recapitulation of this is outside the scope of this paper, but we discuss the consequences of these uncertainties for our study in Section 4.6.

In Table 2 we list the metallicities of the progenitor regions of 34 type II SNe, three type Ib, two type I Ib, three type Ic, and one type Ic-BL from the PTF first-year core-collapse sample. All subsequent analysis is of the type II hosts, for which we have good statistics. We do not include type I Ib SNe in the type II sample because their spectral similarity to type Ib SNe at all but early times can lead to some typing issues, and because previous studies (e.g. Modjaz et al. 2011; Kelly & Kirshner 2012) considered them in the stripped-envelope subclass. We show the metallicity distribution of the type II hosts for several different strong-line metallicity diagnostics using the empirical conversions of Kewley & Ellison (2008) in Figure 2. In subsequent figures, we choose as our scale convention only the N2 diagnostic of Pettini & Pagel (2004).

### 3. CHARACTERIZING THE SPECTROSCOPIC SUBSAMPLE

To investigate whether we have acquired spectra of a representative subsample of the hosts of first-year PTF

CCSNe (Arcavi et al. 2010), we compared the stellar mass and star formation rates of the hosts with and without metallicity estimates. We used SED models of the SDSS photometry of the hosts within the DR8 footprint to estimate the masses, SFR, and characteristic stellar ages. Of the 52 type II SNe in the full sample, 47 have SDSS photometry. We also analyzed the properties of the 19 non-type II PTF CCSN hosts that fell in the DR8 footprint, but we will restrict our comparisons with our spectroscopic sample of type II SNe to these 47 type II SNe to avoid any of the currently known selection effects with metallicity linked with supernova type (see §1).

### 3.1. Extracting fluxes from SDSS imaging

We began with *ugriz* images of the 66 first-year PTF CCSN fields in the SDSS Data Release 8 (Aihara et al. 2011). These images are fully calibrated in the SDSS natural system, which is close to the AB system, and sky-subtracted. We combined the most sensitive SDSS bands (*gri*) for each supernova field in order to make a deeper stacked image that can be used to find all the galaxies and define their photometric apertures. We used these deeper stacked images as the reference image for source detection using SExtractor (Bertin & Arnouts 1996) and checked by eye the positions around each supernova in order to select the most likely host galaxy. We were able to assign likely host galaxies for 64/66 SNe. The two events without host galaxy detections, PTF09be and PTF09gyp, have sources that are  $\gtrsim 13$  kpc (projected) from the positions of the SNe. We note that the host of PTF09gyp has a reported magnitude of  $r = 21.75$  mag in Arcavi et al. (2010) from pre-explosion PTF survey co-adds (I. Arcavi, private communication), but we cannot confirm this detection with DR8, although a galaxy detected approximately 15 arcseconds away has a similar magnitude. After selecting the host galaxies in the stacked images, we used *imedit* in IRAF<sup>6</sup> to mask nearby stars, which could contaminate the flux measurements, filling the masked regions with the local background. Finally, we ran SExtractor on the individual *ugriz* images using the apertures defined from the deeper stacked images to obtain total (AUTO) galaxy fluxes. We applied the small ( $\lesssim 0.04$  mag) corrections derived in Kessler et al. (2009) to transform the SDSS fluxes to the AB system. The resulting coordinates and fluxes of the host galaxies are presented in Table 4, and absolute magnitudes k-corrected and corrected for galactic extinction are presented in Table 5. We include  $3\sigma$  upper limits for the hosts of PTF09be and PTF09gyp, which were calculated assuming a circular aperture of radius  $r = 5$  kpc at the distance of the SN.

### 3.2. Galaxy properties

We used the code for Fitting and Assessment of Synthetic Templates (FAST v0.9b, Kriek et al. 2009) to fit these host galaxy spectral energy distributions to estimate the stellar mass, star formation rates (SFRs), and characteristic ages. We chose the Bruzual & Charlot (2003) libraries, a Salpeter IMF, and Solar ( $Z = 0.02$ )

metallicity to do the fits. We also assumed an exponentially declining SFR model with  $\tau = 1$  Gyr for the star forming component of the model. The results are presented in Table 6.

In order to check the SFRs calculated with FAST, we also estimated SFR based on the results presented by Salim et al. (2007). This method is also based on toy models for the SFR as a function of time, but combines bursts, constant star formation, and exponentially declining star formation, which make it more realistic than FAST. We used the results of Salim et al. (2007) for  $\sim 50000$  SDSS galaxies with GALEX photometry to derive a relation between the absolute *u*-band magnitudes, corrected for intrinsic attenuation, and their derived SFRs. We obtain a linear relation fit between  $M_u$  and SFR (in  $M_\odot/\text{yr}$ ) of the form  $\log(\text{SFR}) = -0.36 \times M_u - 6.73$  (for a Salpeter IMF), valid for  $2 > \log(\text{SFR}) > -2$  and  $\log(\text{SFR}/M_\odot) > -10.5$ , with an rms scatter of 0.23 dex. We applied this relation to obtain SFRs for the supernova host galaxies, using the Low-Resolution Template code of Assef et al. (2008) to derive *K*-corrected *u*-band absolute magnitudes corrected for Galactic extinction. After further correcting these magnitudes by intrinsic attenuation using the values obtained with FAST and the Calzetti reddening law, we applied the linear relation derived from the Salim et al. (2007) data to estimate SFRs. These values are presented in Table 6. The agreement with the SFRs derived by FAST is fairly good in general, with a Kolmogorov-Smirnov (K-S) test probability of 81% of the results of the two different methods being drawn from the same underlying distribution. The two SFR estimation methods are directly compared in Figure 3. The SFR calculated from the *u*-band luminosity with aperture corrections is more consistent with the method the MPA/JHU value-added catalog uses to determine star formation rates than the FAST template fitting.

## 4. RESULTS AND DISCUSSION

This is the largest sample yet of supernova host galaxy spectra metallicity measurements from a single survey. Nevertheless, limited observing time made following up the entire PTF type II sample impractical, so we first show in §4.1 that our spectroscopic host sample is representative of the full sample. We then place the SN hosts in context in §4.2 by comparing their properties to those of galaxies in the MPA/JHU value-added catalog. We find that while they are well-matched in galaxy mass and metallicity, the type II hosts appear to be biased toward higher star formation rates than the galaxies in the catalog. We show in §4.3 that the metallicity distribution of these type II hosts is remarkably similar to that found by previous studies of hosts of type II SNe, despite coming from multiple surveys with different selection functions. Their metallicity distribution is also consistent with a distribution of star formation calculated from galaxy population statistics (§4.4). We discuss in §4.5 how our study avoids some selection effects due to supernova type and host galaxy type that might influence the metallicity distribution. A key future use of the metallicity distribution of type II SNe we find here will be to evaluate possible metallicity dependence of other subclasses of CCSNe. We discuss the advantages and disadvantages of the metallicity diagnostic we choose for

<sup>6</sup> IRAF is distributed by the National Optical Astronomy Observatory, which is operated by the Association of Universities for Research in Astronomy (AURA) under cooperative agreement with the National Science Foundation.

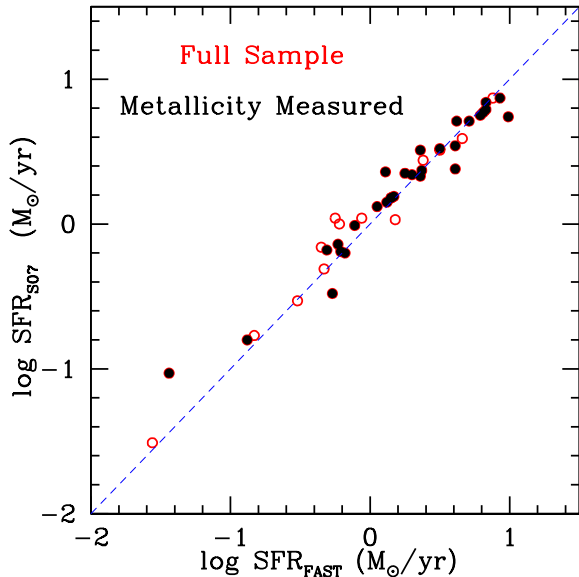


**Figure 3.** The two methods of estimating SFR are consistent. SFR estimates based on  $u$ -band photometry (Salim et al. 2007) are plotted against SFR estimates based on FAST for the full sample of PTF type II SN hosts (open red points) and the metallicity subsample (solid black points). The blue dashed line represents a 1:1 correspondence.

this study in §4.6. Finally, we fit a relationship between oxygen and iron abundances in §4.7, and convert our observed oxygen abundance distribution into an assumed iron abundance distribution, as iron is more important to the evolution of massive stars than oxygen.

#### 4.1. How representative is the metallicity sample?

To investigate how representative the subsample for which we have spectra and metallicities is of the entire sample of PTF type II SN hosts we compared the distributions of the two samples in galaxy mass, characteristic stellar age, and star formation rate, using the 32 (47) hosts with (and without) measured metallicities that also lie in the SDSS DR8 imaging footprint. Figures 4 and 5 show that the two sub-samples have essentially identical distributions in host mass (K-S probability 99.9%), age (57.8%), and SFR (64–74%, depending on the SFR estimation method).

We also investigated the effects of redshift on the completeness of the sample by dividing it into lower and higher redshift subsamples and comparing the properties of the two. In Figure 6 we show the metallicity distribution of these two subsamples. A K-S test indicates that the two have a 19% probability of being drawn from the same metallicity distribution, consistent at approximately  $1\sigma$ . The hosts in the two redshift bins have essentially identical distributions in host mass (K-S probability 63%), age (91%), and SFR (91–99%, depending on the estimation method).

#### 4.2. The type II metallicity sample in context

We next place our type II host sample in context by comparing it to galaxy properties in the DR7 SDSS MPA/JHU value-added catalog (Kauffmann et al. 2003; Tremonti et al. 2004; Brinchmann et al. 2004;

Salim et al. 2007). We compare to the subset of the DR7 objects which have redshifts within the range of our sample, successful estimates of the stellar mass and star formation rate, a  $12+\log(\text{O}/\text{H})$  metallicity estimate, and an  $[\text{N II}]\lambda 6584/\text{H}\alpha\lambda 6563$  flux ratio within the valid range for the PP04 N2 metallicity diagnostic. This last requirement has almost no effect, reducing the sample by only 0.6%. The strictest condition by far is the requirement of a valid Tremonti et al. (2004) metallicity estimate, as shown in Table 7. Note that the galaxy properties in the MPA/JHU value-added catalog are a function of redshift because is not a volume-limited sample. The selection that defines the catalog is reflected in the properties of its constituents.

As shown in Figure 7, the SN hosts appear to trace the MPA/JHU sample well. Their mass-metallicity relationships are consistent at approximately one sigma. Strong conclusions should not be drawn from this, as the sample selection functions of the PTF type II host galaxies and the SDSS galaxy mass-metallicity sample of the MPA/JHU value-added catalog are each complex and based in part on parameters unrelated to the galaxies themselves. The fiber allocation in SDSS prioritized galaxies lower than other target classes, including brown dwarfs and quasar candidates (e.g. Blanton et al. 2003), meaning that the selection function of galaxies observed spectroscopically in a given field is mediated by the density of other targets in that field rather than a simple function of the properties of the galaxies themselves. To zeroth order, SDSS galaxy spectroscopic observations are a function of stellar mass, while core-collapse supernovae (and by extension our host sample) are instead a function of star formation rate in the recent past. Inclusion in the mass-metallicity sample of the MPA/JHU value-added catalog is not a simple function of the galaxy having been spectroscopically observed. In order to be included, the galaxy must have a reasonable fit using the group’s Bayesian metallicity determination. The strength of the spectroscopic features that enable this determination is greater for galaxies with a higher star formation rate, which means that the star formation rate is to a certain extent a hidden parameter in this selection function. The PTF followup selection function is unpublished, and therefore impossible to model. Reconciling the selection functions of these samples sufficiently to draw strong conclusions based on comparing their mass-metallicity slopes is not possible, nor is it the aim of this study. Instead, we compare them to place our results in context.

The SDSS galaxy spectra are primarily nuclear spectra but not exclusively so. In contrast, 50 of locations more than 3 arcsec away from the nucleus, as can be seen in Table 2. The SN location was within 3 (4,6) arcsec of the galaxy center in all but 5 (3,1) of the remaining cases. In one case (PTF09aux), we were unable to measure  $[\text{N II}]$  and  $\text{H}\alpha$  with sufficient S/N to measure metallicity. Type II SNe have no known metallicity dependence, so they are not expected to favor the outer, more metal-poor regions of galaxies.

Although quantitative conclusions should not be drawn from this similarity due to these unavoidable sample selection incongruities, some qualitative conclusions can be drawn. The type II SN hosts do not appear to be biased toward lower metallicities at a given mass (left panel) as a simplistic interpretation of the results of

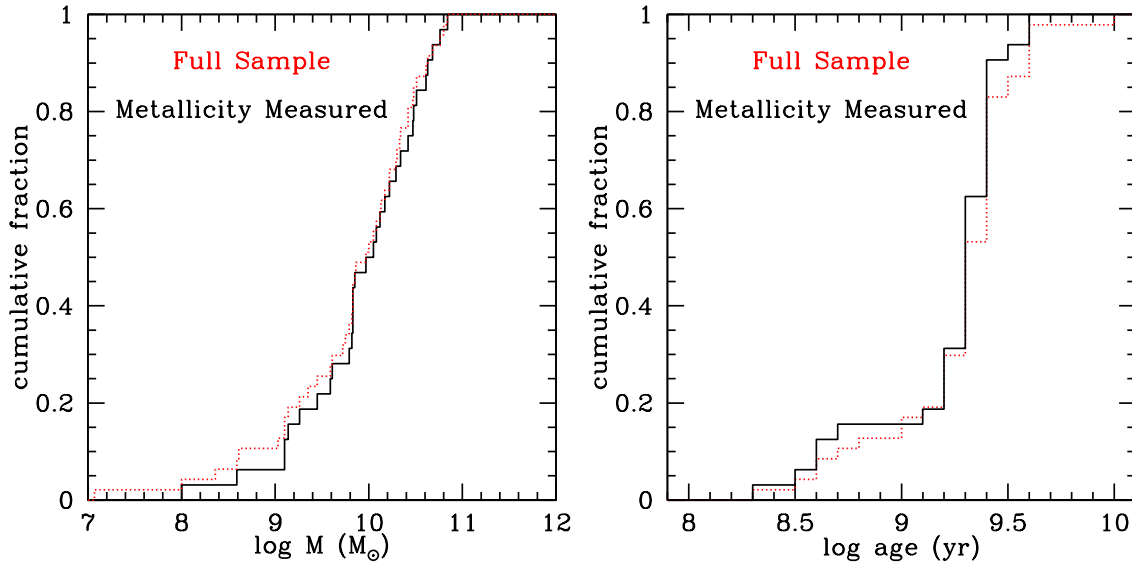


**Figure 4.** The distributions of the full PTF type II sample (dotted red) and those for which we obtained metallicities (solid black). Section 3.2 describes how the host properties were estimated. The subsample for which we have spectroscopic metallicity measurements is quite representative of the full sample, with K-S test probabilities of 99.9% (mass) and 57.8% (age) that they are drawn from the same distribution.

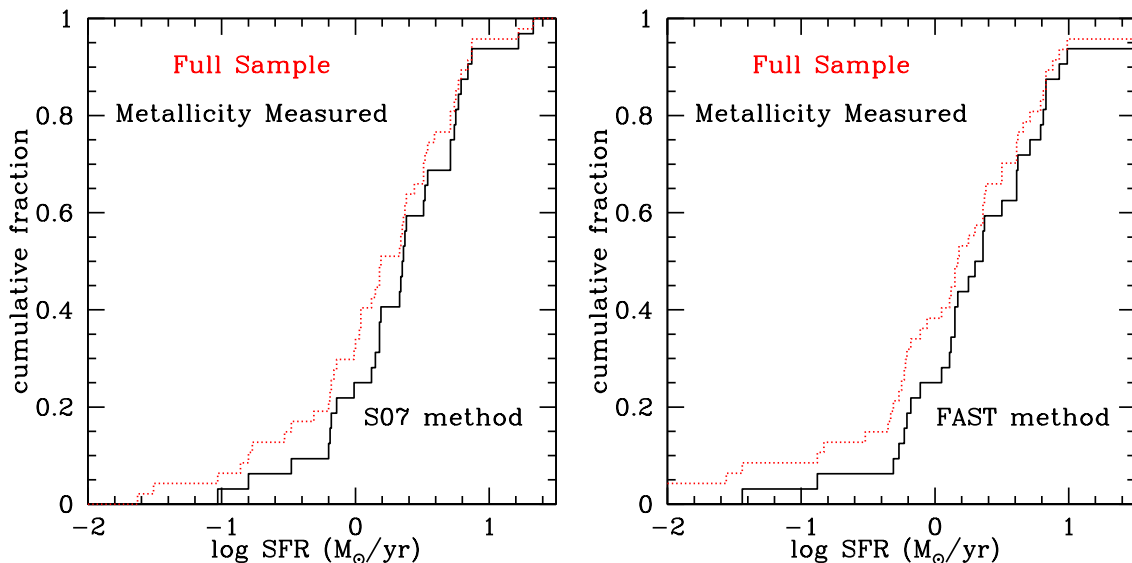


**Figure 5.** The subsample of type II hosts for which we have measured metallicities (solid black) is representative of the full sample of PTF type II SN hosts (dotted red) in SFR based on  $u$ -band photometry (Salim et al. 2007, left) and FAST (right).

Mannucci et al. (2010) might suggest. It has been suggested that core-collapse SNe and GRBs may be less frequently observed in higher metallicity environments than in lower metallicity environments due to higher extinction (e.g. Maiolino et al. 2002; Mannucci et al. 2003; Cresci et al. 2007; Campisi et al. 2011), but this sample does not show evidence for such a bias. The SN hosts do, however, appear to be biased toward higher star formation rates<sup>7</sup> (right panel) than the MPA/JHU galaxy sample, as would be expected if they do indeed trace

<sup>7</sup> Here we use the SFR calculated from the  $u$ -band luminosity with aperture corrections.

star formation. They appear to trace the distribution of the MPA/JHU sample well in galaxy mass and star formation rate, as shown in Figure 8.

#### 4.3. Comparing with other SNe host samples

Work on the metallicity distribution of supernova hosts by Prieto et al. (2008) and Kelly & Kirshner (2012) looked at overall galaxy metallicity with serendipitous SDSS spectra, without isolating the SN site. Kelly & Kirshner (2012) subdivide their sample into those discovered by galaxy-impartial searches and by targeted searches. Studies by Anderson et al. (2010) tried to measure abundances at the SN site or at a similar

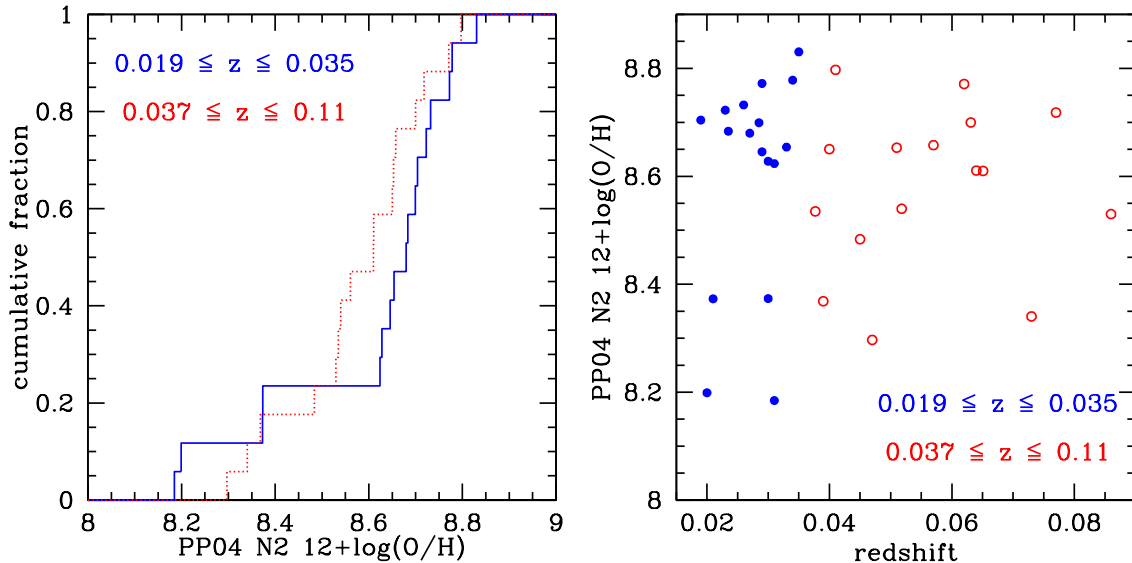


**Figure 6.** The metallicity distribution of the type II hosts separated into two bins in redshift of seventeen hosts each (left). The green solid (red dotted) line is the lower (higher) redshift half of the sample,  $0.019 \leq z \leq 0.035$  ( $0.037 \leq z \leq 0.11$ ). On the right, the distribution is expanded and metallicities are plotted against redshift. Here the lower redshift half of the sample is green solid points, and the higher redshift is red open points. A K-S test shows the two are consistent with being drawn from the same distribution in metallicity at the 19% level. There do not appear to be any major selection effects with redshift.

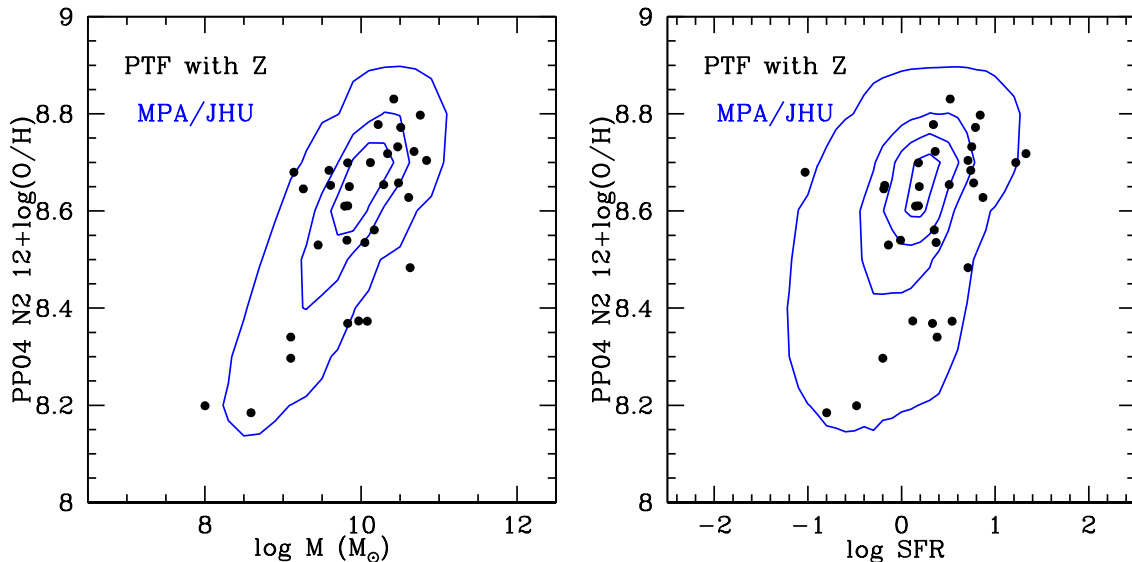


**Figure 7.** Measured host metallicities (black points) as a function of galaxy mass (left) or SFR (right), overlaid on the distribution in the MPA/JHU value-added catalog in the same redshift range (blue contours). Our hosts are slightly offset to higher star formation rates, as we would expect if type II SNe trace star formation.

galactocentric radius, as we have done in this study. These previous studies had uniform spectroscopy but the source SN samples were heterogeneous, including SNe discovered in a wide variety of ways with very different selection effects. Our source SN sample is from a single survey with uniform selection. The source survey is areal rather than galaxy-targeted, which enables the detection of events in the lowest-mass galaxies, removing or at least mitigating a possible bias towards high metallicity environments which we expect exists in prior supernova host samples. We do not attempt to define a

volume-limited supernova sample here. Rather, we point out that this existing sample represents a substantial step forward from previous similar samples for the purpose of providing a comparison for a non-matched sample of rare core-collapse events, particularly one thought to depend on metallicity such as GRBs or abnormally luminous CC-SNe.

Kelly & Kirshner (2012) used abundances following Tremonti et al. (2004) and the O3N2 method of Pettini & Pagel (2004). In this paper we use the N2 method of Pettini & Pagel (2004), so we must convert

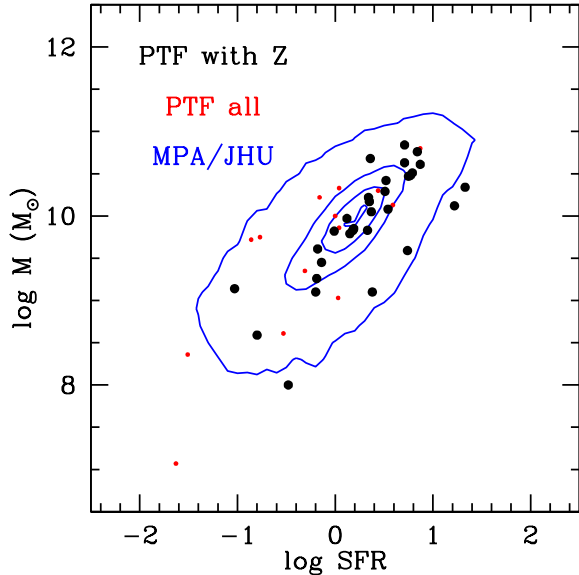


**Figure 8.** Host mass and SFR for our type II SN hosts with Z measurements (large black points), all first-year PTF type II SNe hosts in the SDSS photometric footprint (small red points), overlaid on the distribution in the MPA/JHU catalog (blue contours).

these to a common scale. The valid range of the conversion defined by Kewley & Ellison (2008) from the scale of the O3N2 method to the scale of the N2 method does not span the abundances here, so we omit three of the 124 hosts in the sample, and convert from O3N2. Prieto et al. (2008) uses abundances from the method of Tremonti et al. (2004), we omit the 14 of 152 hosts that have T04 metallicities above or below the valid conversion range defined by Kewley & Ellison (2008).

We compare our type II host metallicity distribution with those found by Prieto et al. (2008), Kelly & Kirshner (2012) targeted (T) and galaxy-impartial (I), and Anderson et al. (2010) in Figure 9. The K-S test probabilities that our type II sample could be selected from the same underlying distribution as those in the earlier studies are 43%, 68%, 4%, and 21%, respectively. The agreement of our SN metallicity distribution with the results of these prior studies is striking, given the different sample selection. The most different sample (at a K-S probability of only 4%) is the one which would seem to be the most similar; the heterogeneous galaxy-impartial sample from Kelly & Kirshner (2012).

#### 4.4. Comparing with SFR metallicity distributions from galaxy population statistics

One semi-observational way of determining the global distribution of star formation as a function of metallicity is to combine the observed galaxy mass function, the observed mean star formation rate as a function of galaxy mass, and the observed galaxy mass-metallicity relationship. Stanek et al. (2006) combines the 2MASS and SDSS galaxy stellar mass function from (Bell et al. 2003) with the Tremonti et al. (2004) mass-metallicity relation and the Brinchmann et al. (2004) star formation rate density. Niino (2011) calculates the metallicity distribution of star formation two different ways; first, observationally from the stellar mass function, the galaxy M-

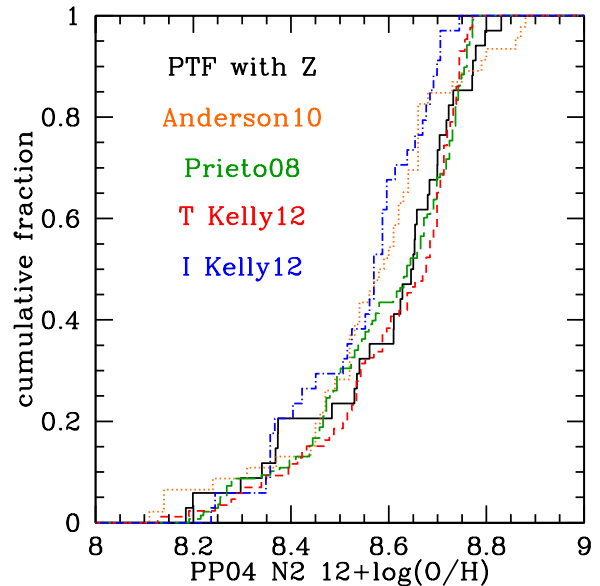


**Figure 9.** Distribution of local gas-phase oxygen abundance of our sample of type II SNe (black solid line) compared with existing SN host metallicity samples. The dotted orange curve shows the heterogeneous type II subsample of Anderson et al. (2010). The K-S probability of this sample being drawn from the same underlying distribution as our PTF type II sample is 11%. Similarly, the green long-dash curve shows the distribution of type II, IIP, and IIc SNe from Prieto et al. (2008) (K-S probability 87%) and the purple dash-dot curve shows the type II sample from Kelly & Kirshner (2012) (K-S probability 45%). In the latter two cases we converted their T04 scale metallicity to the PP04N2 scale using the conversion given in the Appendix.

SFR relation, and the galaxy mass-metallicity relation, nearly identically to Stanek et al. (2006) except using the mass-metallicity relation of Savaglio et al. (2005), and second, calculated using the relationship between galaxy mass, metallicity, and SFR defined by Mannucci et al. (2010), and assigning metallicities based on SFR as well as mass. Each of the three observed relationships that are inputs to these alternate methods of finding the metallicity distribution of star formation has its own set of selection effects. Potential biases or redshift-dependent effects in the samples used to define the relation could offset the distribution in metallicity. The width of the distribution may be misrepresented by using a mean relationship to translate from one property into another, such as the mass-metallicity relationship (Tremonti et al. 2004) or the three-way relationship between mass, metallicity, and star formation rate (Lara-López et al. 2010; Mannucci et al. 2010), because the scatter around that relationship may not be carried through to the final distribution.

In Figure 10 we plot our distribution against those of Stanek et al. (2006) and Niino (2011) based on galaxy population statistics. We convert the metallicities using Kewley & Ellison (2008). The non-monotonicity of the conversions from T04 and KK04 to PP04N2 results in non-physical double-values in the cumulative distributions. On the right, metallicity conversions are done with by inverting the reverse conversions, as described in Appendix. This maintains the physicality of the distribution function, but may increase inaccuracy at higher

metallicities. Because the forward and reverse conversions do not match, multiple conversions between metallicity scales will compound errors. This is likely the reason why the distribution from Stanek et al. (2006) (in green) does not match the distribution from Niino (2011) which considers the mass-metallicity relation independently of star-formation (in red). Instead of using Tremonti et al. (2004), Niino (2011) uses the mass-metallicity relation of Savaglio et al. (2005) on the KK04 scale, though they are otherwise identical.

Core-collapse SNe, as the deaths of massive, young stars, are a relatively good tracer of SFR. Using the metallicity distribution of a uniform sample of type II SN sites to approximate the metallicity distribution of star formation, as we have done, should have almost completely independent selection effects (such as extinction from dust) from methods relying on galaxy population statistics.

#### 4.5. Selection effects

One of the primary potential sources of incompleteness in using type II SNe environments to trace the metallicity distribution of global star formation will of course be the selection of the sample of type II SNe. An ideal sample for this purpose would be a complete, volume-limited sample, monitoring a fixed region of sky for a fixed period of time, and then eliminating events outside the complete sample. Up until very recently, most supernova surveys have monitored large, luminous galaxies rather than regions of the sky, a methodology which has the potential to miss any SNe in the very lowest end of the galaxy luminosity function. The Palomar Transient Factory survey is areal, which removes the potential bias against extremely low-mass host galaxies of targeted surveys. Because the survey selection is not yet published, however, we are unable to correct for any biases in our source sample to get a distribution for a volume-limited sample. With the current rapid growth in depth and breadth of supernova surveys, there is great potential for this method of determining the metallicity distribution of star formation.

Another potential source of bias for this method is any dependence of the likelihood of a massive star resulting in a type II SN on metallicity. Type II-P SNe make up around 70% of all type II SNe in the LOSS survey, which focuses on relatively luminous galaxies (Li et al. 2011). The relative frequency of type II SNe has not yet been found to depend on metallicity, unlike type Ib and Ic SNe. We examine only the distribution of type II hosts, for which we have good statistics. The type II distribution is consistent with the distribution of the nine type Ib/Ic/IIb hosts we have measured with a K-S probability of 23%, and the distribution of the hosts of all CCSNe we have measured (including all the type II hosts) is consistent with the type II distribution with a K-S probability of 99%, shown in Figure 11 (left). Completeness corrections to translate between type II hosts and all CCSN hosts may depend slightly on metallicity.

Several types of CCSNe are known to vary in frequency with metallicity, as discussed in §1. Our very small sample of spectroscopic metallicity measurements of hosts of type IIb/Ib/Ic SNe is statistically consistent with these previous results (Modjaz et al. 2011; Anderson et al. 2010; Kelly & Kirshner 2012), but not

at very high significance level. Using the host galaxy properties we fit from SDSS photometry gives us slightly better statistics, shown in Figure 11 (right). The over-representation of types IIb and Ic-BL in low-mass hosts is consistent with the results of Arcavi et al. (2010) of this same sample based on host galaxy luminosities, but again, not at very high significance. The relative distributions of type II, IIb, Ib, Ic, and Ic-BL in photometrically calculated host mass are consistent with the recent results of Kelly & Kirshner (2012).

#### 4.6. Strong-line metallicity diagnostics

There is a substantial literature on the merits and disadvantages of each commonly-used method of determining metallicities based on fluxes of strong emission lines (e.g. Berg et al. 2011; Kewley & Ellison 2008, and references therein). These methods all rely on simplifying assumptions about the H II regions being examined: uniformity of electron density, cooling dominated by oxygen (implying that other cooling species have abundances that vary in lockstep with oxygen), and ionization-bounded H II regions (e.g. Pagel et al. 1979). The methods can be classified into rough categories: direct methods, which rely on estimates of the electron temperature and require measurements of faint auroral lines such as  $[\text{O III}]\lambda 4363\text{\AA}$ , empirical (e.g. Pettini & Pagel 2004), theoretical (e.g. Kobulnicky & Kewley 2004), and a combination of empirical and theoretical (e.g. Denicoló et al. 2002). All these methods are based on high S/N measurements of the line ratios of different combinations of emission lines from ions present in the optical region of the spectrum ( $\simeq 3700 - 6800\text{\AA}$ :  $[\text{O II}]$ ,  $[\text{O III}]$ ,  $[\text{N II}]$ ,  $[\text{S II}]$ ,  $\text{H}\alpha$ , and  $\text{H}\beta$ ).

The slope and intercept of the galaxy mass-metallicity relationship is different for each diagnostic (Kewley & Ellison 2008), which is a relatively straightforward way to demonstrate that they are not all directly measuring some platonic ideal of a fundamental oxygen abundance measurement. (This problem is independent of the separate question of the exact value of the solar oxygen abundance, which also affects how measured gas-phase abundances map to stellar abundances.) Instead, each technique measures a different quantity that correlates well with oxygen abundance, but does not directly map to it. The simplifying assumptions that allow us to use each strong-line indicator to estimate oxygen abundance are not perfect for all H II regions. Rigorously selecting the best diagnostic for a given situation requires better data than are achievable for distant and faint targets, and doing a case-by-case selection of strong-line method on insufficient data would introduce its own biases.

The primary advantage of the strong-line techniques is that they are possible with fewer photons, and are therefore feasible to perform on large samples for good population statistics. Given the scale differences between methods, however, it is crucially important to ensure that all metallicities one is comparing are on the same scale. Where possible, we do this by natively determining the metallicities in a common scale. Where impossible, we convert a metallicity determined on another scale using the empirical conversions of Kewley & Ellison (2008) (but see Appendix A). We emphasize that any meaning-

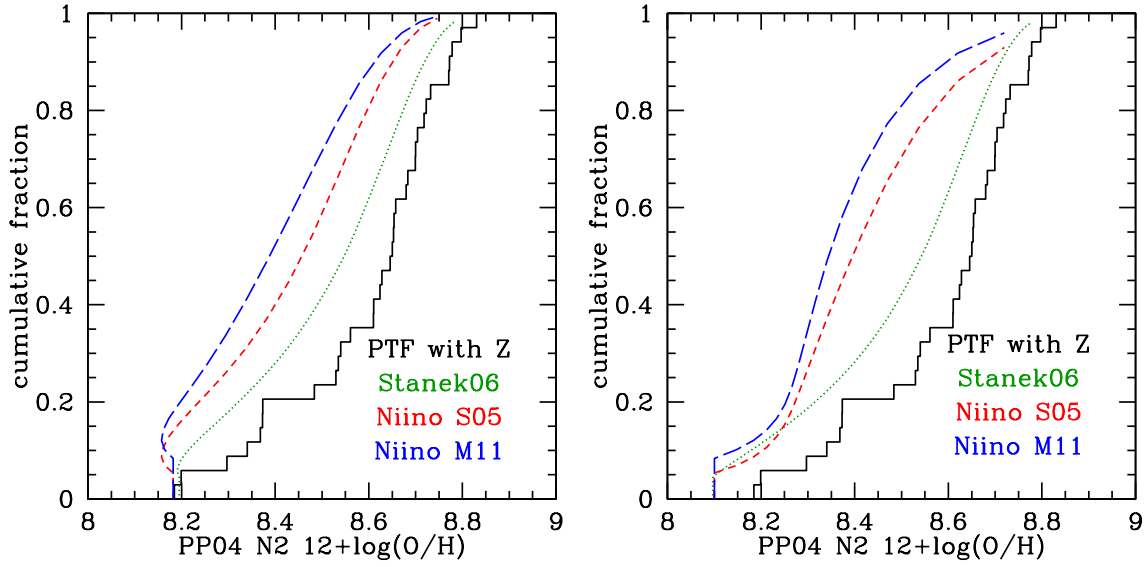


**Figure 10.** The distribution of star formation as a function of metallicity from galaxy population statistics from Staneck et al. (2006) (green dotted line) and Niino (2011) with (blue long-dashed line) and without (red short-dashed line) incorporating the star-formation-rate dependence of the mass-metallicity relationship as Mannucci et al. (2010), compared to our distribution of site metallicities of type II CCSNe (black solid line). On the left, the metallicity conversions were made with Kewley & Ellison (2008). The non-monotonicity of the conversions from T04 and KK04 to PP04N2 results in the non-physical double-values. On the right, conversions are done with by inverting the reverse conversions, as described in Appendix. This maintains the physicality of the distribution function, but may increase inaccuracy at higher metallicities.

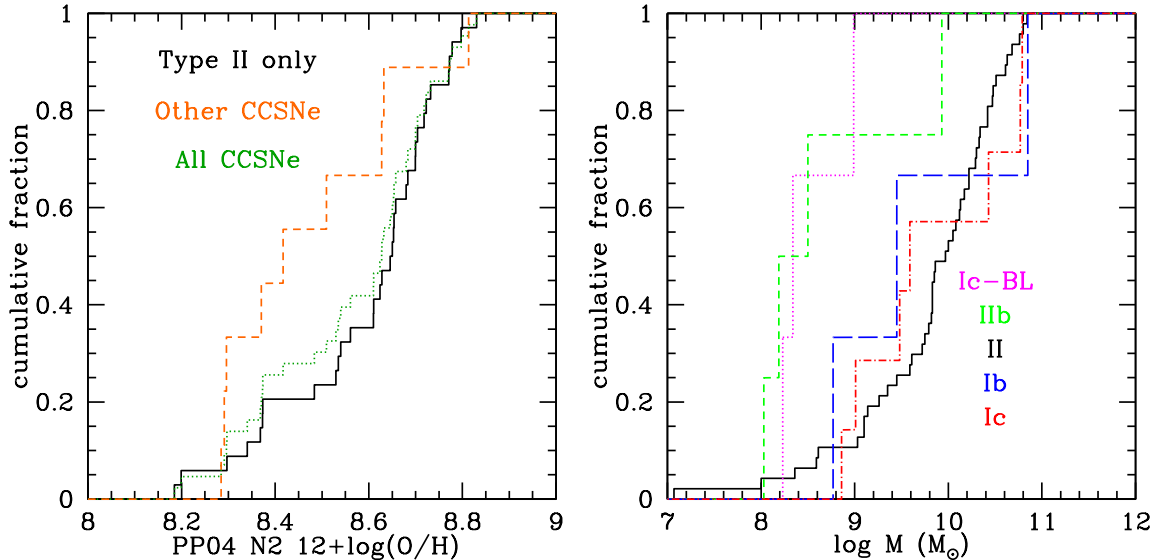


**Figure 11.** The metallicity distribution (left) of type II SN hosts (solid black), all other CCSN hosts (dashed orange) and all CCSN hosts in Table 2 (dotted green). With this small sample of other subtypes, the type II distribution is statistically consistent with the other CCSNe (K-S probability 23%) and with all CCSNe (K-S probability 99%). Increasing the sample size, the distribution in photometrically calculated host galaxy mass (right) of type II SN hosts (black solid), Ic-BL (pink dotted), IIb (green short-dashed), Ib (blue long-dashed), and Ic (red dot-dashed). These distributions are consistent with the overrepresentation of IIb and Ic-BL at low host luminosity found by Arcavi et al. (2010) and with the distributions in host mass found by Kelly & Kirshner (2012).

ful conclusion should not be affected by a change in the metallicity calibration.

The primary scale we choose for this study is the N2 diagnostic of Pettini & Pagel (2004), which depends solely on  $[\text{N II}]\lambda 6584/\text{H}\alpha\lambda 6563$ . Three disadvantages of the method are that it shows a larger dispersion compared to the direct ( $T_e$ ) method than most other strong line diagnostics, that it has a dependence on the ionization parameter that becomes important at low metallicities (PP04N2  $12+\log(\text{O}/\text{H}) < 8.0$ ) (López-Sánchez et al. 2012), and that it loses sensitivity and saturates at high metallicities (PP04N2  $12+\log(\text{O}/\text{H}) > 8.86$ ). There are a number of key advantages of this diagnostic, however. The ratio is very insensitive to reddening due to the close wavelength proximity of the lines. It is monotonic with oxygen abundance. It depends on lines with relatively high fluxes in star forming environments, which means that good metallicity estimates can be achieved at relatively low observational expense. Yin et al. (2007) find it is more consistent with  $T_e$  methods than the O3N2 diagnostic of Pettini & Pagel (2004), and Bresolin et al. (2009) compare a variety of strong-line abundance estimators and find that PP04N2 is the closest match in both slope and normalization to the oxygen abundance gradient in NGC 300 measured with the  $T_e$  method and measured with stellar metallicity (blue supergiants).

#### 4.7. Iron abundances

Iron is more important than oxygen for the late-stage evolution of massive stars, because iron provides much of the opacity for radiation-driven stellar winds (Pauldrach et al. 1986; Vink & de Koter 2005, e.g.). Unfortunately, gas-phase iron abundances are difficult to measure, and the fraction of iron depleted onto grains is highly variable. Even within our own galaxy, measuring iron abundances is challenging (e.g. Rodríguez 2002; Jensen & Snow 2007; Okada et al. 2008). We measure gas-phase oxygen abundances instead as a proxy for metallicity because it is observationally feasible.

Because iron is the dominant opacity source, we would like to estimate the iron abundances implied by the observed oxygen abundances. To do this we make use of three correlations: first, the PP04N2 diagnostic, which uses a function of the flux ratio of the  $\text{H}\alpha$   $\lambda 6563$  and  $[\text{N II}]\lambda 6584$  lines that correlates well with direct method ( $T_e$ ) measures of gas-phase oxygen abundance; second, the tight correlation of direct method measures of gas-phase oxygen abundance with stellar oxygen abundance; third, the correlation between stellar oxygen and stellar iron abundances.

Bresolin et al. (2009) find that PP04N2 is the closest match in both slope and normalization to the oxygen abundance gradient in NGC 300 measured with  $T_e$  methods, with an average error of approximately 0.1 dex. Although PP04N2 is a good match to direct-method gas-phase oxygen abundance, it is not perfect, and a small correction to slope and zero point could be made. For the purpose of this paper, however, we assume that PP04N2 maps precisely to direct-method oxygen abundances. Bresolin et al. also find that the gas-phase oxygen abundance gradient measured with  $T_e$  methods correlates very tightly with the stellar oxygen abundance gradient, with an error of no more than about 0.03 dex. For the purposes of this paper, we assume that the

correspondence between  $T_e$  gas-phase oxygen abundance and stellar oxygen abundance is one-to-one, which is a very good assumption.

Stars that have low oxygen abundances have even lower iron abundances. At low metallicity,  $\alpha$ -elements like oxygen are enhanced relative to iron compared to the solar mixture. In the galactic disk and halo, at  $[\text{Fe}/\text{H}] > -1$ ,  $[\text{O}/\text{Fe}]$  is approximately inversely proportional to  $[\text{Fe}/\text{H}]$ , as can be seen in the left panel of Figure 12, while below  $[\text{Fe}/\text{H}] = -1$ ,  $[\text{O}/\text{Fe}]$  may flatten out at a constant (and lower) relative iron abundance (e.g. Tinsley 1979; McWilliam 1997; Johnson et al. 2007; Epstein et al. 2010) (but see e.g. Israelian et al. 1998).

To estimate the conversion between stellar oxygen and iron abundance, we compared  $[\text{O}/\text{H}]$  to  $[\text{Fe}/\text{H}]$  over a wide range in metallicities using stellar abundance measurements from the Milky Way bulge, disk, and halo, from Fulbright et al. (2007); Rich et al. (2007); Rich & Origlia (2005); Lecureur et al. (2007); Reddy et al. (2003, 2006); Bensby et al. (2004); Chen et al. (2003). We fit the relationship between  $[\text{O}/\text{H}]$  and  $[\text{Fe}/\text{H}]$  with an unweighted linear fit, as seen in Figure 12, and find

$$[\text{Fe}/\text{H}] = c_1 + c_2([\text{O}/\text{H}]), \quad (1)$$

where  $c_1 = -0.34 \pm 0.01$  and  $c_2 = 1.25 \pm 0.05$ . Although the eye is drawn to a steeper trend at higher metallicity than the formal fit shown, this misleading and based on relatively few points; the fit is driven to be flatter by a dense concentration of points with  $-0.2 < [\text{O}/\text{H}] < 0.2$  and  $-0.5 < [\text{Fe}/\text{H}] < 0$ . The relationship does not differ substantially between bulge stars (shown in red) and halo and disk stars (shown in blue). If  $[\text{O}/\text{Fe}]$  flattens out below  $[\text{Fe}/\text{H}] = -1$ , the linear relationship we choose to fit may not extend to lower metallicities. We would expect to find a slightly steeper relationship were we to exclude points below  $[\text{Fe}/\text{H}] = -1$ , which would mean that type II SN progenitors in low oxygen abundance host regions have even lower iron abundance than we find here. Because there is finite scatter in the measured relationship, however, imposing a strict cut at  $[\text{Fe}/\text{H}] = -1$  actually drives the fit to be slightly flatter by biasing the points with lowest  $[\text{O}/\text{H}]$  to higher  $[\text{Fe}/\text{H}]$ . The exact value of the slope is not critically important; the main point is that low oxygen abundances imply even lower iron abundances, as can easily be seen in the right side of Figure 12. This is equivalent to saying that at low metallicities, alpha elements are enhanced relative to iron.

Stellar abundances are measured relative to solar, while gas-phase abundances are (nominally) absolute. Applying the fit to a direct conversion between  $12+\log(\text{O}/\text{H})$  and  $[\text{Fe}/\text{H}]$  therefore requires assuming a solar oxygen abundance. There is currently some dispute over the solar abundance because results from atmospheric and interiors methods differ. For a given solar oxygen abundance  $O_\odot$ ,

$$[\text{Fe}/\text{H}] = c_1 - c_2 O_\odot + c_2(12 + \log(\text{O}/\text{H})). \quad (2)$$

Using a solar oxygen abundance of  $O_\odot = 8.86$  (Delahaye & Pinsonneault 2006), the conversion is  $[\text{Fe}/\text{H}] = -11.4 + 1.25(12 + \log(\text{O}/\text{H}))$ , while using  $O_\odot = 8.69$  (Asplund et al. 2009), the conversion is  $[\text{Fe}/\text{H}] = -11.2 + 1.25(12 + \log(\text{O}/\text{H}))$ .

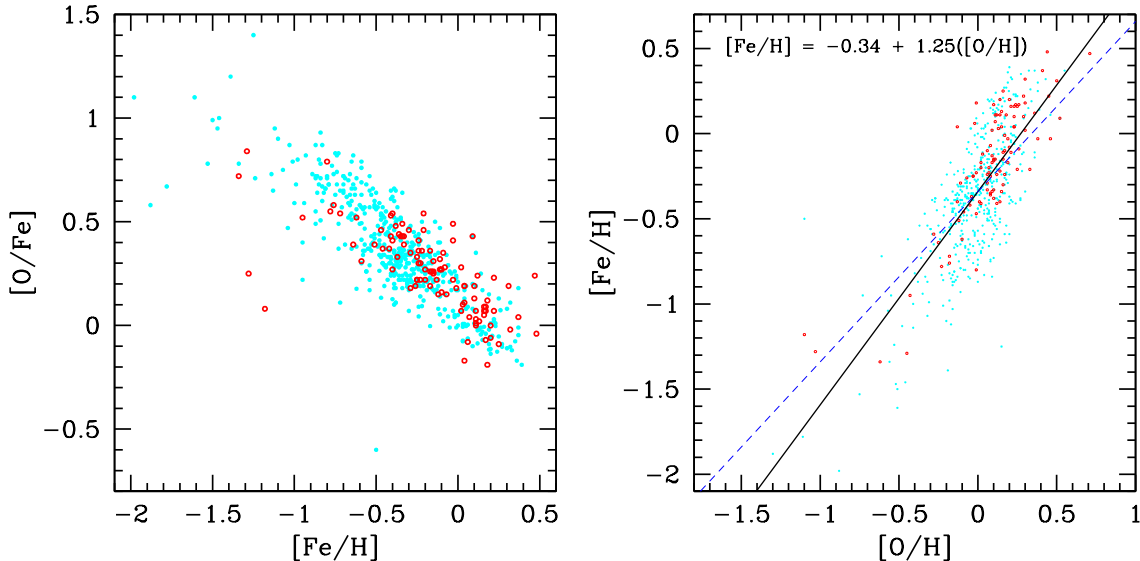


**Figure 12.** To translate oxygen abundances into iron abundances, we fit a linear relation (black) to the iron and oxygen abundances of Milky Way bulge, disk, and halo stars. At low metallicity,  $\alpha$ -elements like oxygen are enhanced relative to iron compared to the solar mixture. On the left is the well-known relationship between  $[O/Fe]$  and  $[Fe/H]$ . The red open points are iron and oxygen abundances of bulge stars (Fulbright et al. 2007; Lecureur et al. 2007; Rich & Origlia 2005; Rich et al. 2007). The blue solid points are halo and disk stars (Bensby et al. 2004; Chen et al. 2003; Reddy et al. 2003, 2006). On the right we express this in terms of  $[O/H]$  and  $[Fe/H]$  and fit the relation. Although the eye is drawn to a steeper trend at higher metallicity than the formal fit, this is an illusion based on relatively few points; the fit is driven to be flatter by a dense concentration of points with  $-0.2 < [O/H] < 0.2$  and  $-0.5 < [Fe/H] < 0$ . The blue dashed line has a slope of 1 to guide the eye and intersects with the fit at  $[O/H] = 0$ , showing that iron varies more steeply than oxygen. If the slope is steeper than we have fit, this conclusion strengthens. Equation 2 can be used to conservatively convert a measured gas-phase oxygen abundance to iron abundance for a given solar oxygen abundance (modulo the uncertainties of equating gas-phase strong-line oxygen abundance indicators to stellar oxygen abundances). This conversion is necessary because at low metallicities, alpha elements such as oxygen are enhanced relative to iron, and iron is the main opacity source for line-driven winds and thus may drive mass loss for supernova progenitors.

We apply this fit to transform our oxygen abundance distribution of type II progenitors into an iron abundance distribution, shown in Figure 13. The median value of  $[Fe/H]$  is  $-0.60$  using the solar value of Delahaye & Pinsonneault (2006). If another solar oxygen abundance  $O_{\odot}$  is assumed, the calculated iron value shifts by

$$c_2(8.86 - O_{\odot}), \quad (3)$$

so using  $O_{\odot} = 8.69$  (Asplund et al. 2009), for example, the median value of  $[Fe/H]$  is  $-0.39$ .

The most important result here is that the gap between the iron and oxygen abundances is 50% wider at the low-metallicity end of the distribution than at the high-metallicity end, even though this sample spans less than a dex in abundance. Were we to assume that  $[O/Fe]$  flattens out below  $[Fe/H] = -1$  instead of remaining linear, the slope we fit would be steeper and the difference would be even greater. A striking outcome of this translation is that all of the type II SN progenitors in this sample appear to have sub-solar iron abundances. Although this is notable, it is not entirely surprising; the sun is more enhanced in iron than most Milky Way stars at its oxygen abundance, and all of the host galaxies in this sample are smaller than the Milky Way. It is, however, not a secure result. Given the scatter in the correlations we use to define this relation, we caution that conversions of average values are uncertain at the level of at least 0.15 dex, and conversions of individual values are uncertain at the level of approximately 0.3 dex.

The type II progenitors all have iron abundances

greater than  $[Fe/H] = -1.5$ , putting them squarely in the regime where winds are primarily driven by iron opacity. For the most metal-poor stars ( $Z/Z_{\odot} < 10^{-3}$ ), non-iron elements such as carbon dominate the radiative driving (Vink & de Koter 2005), but in the metallicity range of these type II SN progenitors, iron abundance should still be the dominant factor which determines wind strength and mass loss.

## 5. CONCLUSIONS

The primary result of this paper is a new progenitor region metallicity distribution for a uniform (though not completely unbiased) sample of type II SNe. Understanding the underlying distribution is important for understanding any possible metallicity dependences of different types of events associated with massive stars, and it can serve as a probe of the metallicity distribution of star formation.

The host galaxies of our type II sample appear to trace galaxies from the MPA/JHU value-added catalog in mass and metallicity, showing a slight bias towards higher star formation rates.

We find a similarity between the existing host metallicity distributions for heterogeneous type II supernova samples and the metallicity distribution we derive. Because the existing host metallicity distributions are based on supernova samples that are drawn predominantly from galaxy-targeted supernova searches, one might naively expect these previous distributions might be biased towards higher mass and therefore higher metallicity galaxies. We do not find such a trend.

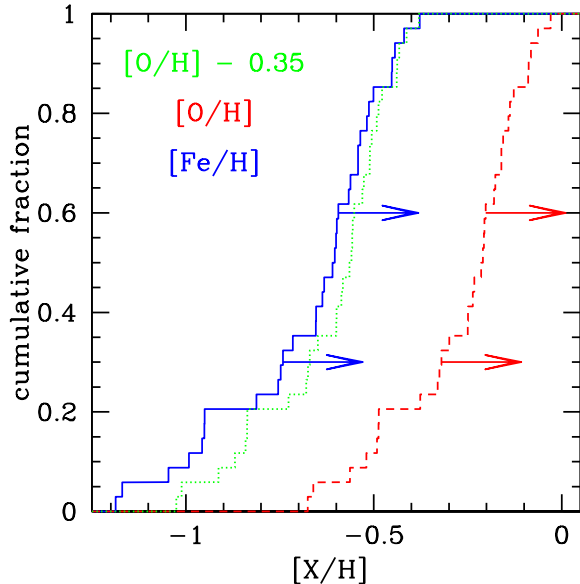


**Figure 13.** The estimated  $[\text{Fe}/\text{H}]$  distribution of the type II SN sites. The red dashed line is the  $[\text{O}/\text{H}]$  distribution, and the blue solid line is the  $[\text{Fe}/\text{H}]$  distribution assuming the solar oxygen abundance is 8.86 (Delahaye & Pinsonneault 2006). The arrows indicate the shift corresponding to assuming a solar oxygen abundance of 8.69 (Asplund et al. 2009). The green dotted line is the oxygen abundance shifted left by 0.35 to line up with the iron at the high-metallicity end. Notice that the gap between the iron and the oxygen abundance is 50% wider at the low-metallicity end of the distribution as at the high-metallicity end. Iron varies more steeply than oxygen, and a galaxy that has low oxygen abundance has even lower iron abundance.

Comparing to the metallicity distribution of star formation rather than to the metallicity distribution of galaxies as a function of mass is the correct way to evaluate a possible metallicity dependence of a transient population associated with young stars. We point out that using CCSNe to trace star formation leads to an almost entirely independent way of probing the metallicity distribution of star formation from methods involving galaxy population statistics, and we compare the metallicity distribution we derive to one of these.

Finally, we present our host metallicity distribution in terms of iron abundance, by converting our oxygen abundance distribution to an iron abundance distribution using the  $\alpha/\text{Fe}$  relationship observed in Milky Way bulge, disk, and halo stars, noting that iron is more important than oxygen for the late-stage evolution of massive stars. We show that even though these hosts span less than

a dex in oxygen abundance, the gap between their iron abundance and oxygen abundance nearly doubles at the low-metallicity end compared to the high-metallicity end. We estimate that  $-1.2 < [\text{Fe}/\text{H}] < 0$  for these type II SN progenitors. Though all may have sub-solar iron abundance, none are metal-poor enough that elements other than iron will dominate the wind-driving opacity of the progenitor star.

Future improvements to this estimate of the metallicity distribution of type II SNe can be made by performing completeness corrections for any selection or followup biases in the source survey. If the peak luminosity of type II SNe is found to depend on host galaxy metallicity, there may also be Malmquist-like biases to correct.

We thank B. Andrews, J. Antognini, R. Assef, D. Atlee, C. Epstein, J. Johnson, C. Kochanek, P. Martini, and L. Watson for discussion, comments, or assistance. RS is supported by the David G. Price Fellowship in Astronomical Instrumentation and the Tuttle Endowment. JLP acknowledges support from NASA through Hubble Fellowship grant HF-51261.01-A awarded by the STScI, which is operated by AURA, Inc. for NASA, under contract NAS 5-26555. This paper uses data taken with the OSMOS spectrograph, built with funding from NSF grant AST-0705170 and from the Center for Cosmology and AstroParticle Physics at The Ohio State University. Funding for SDSS-III has been provided by the Alfred P. Sloan Foundation, the Participating Institutions, the National Science Foundation, and the U.S. Department of Energy. The SDSS-III web site is <http://www.sdss3.org/>. SDSS-III is managed by the Astrophysical Research Consortium for the Participating Institutions of the SDSS-III Collaboration including the University of Arizona, the Brazilian Participation Group, Brookhaven National Laboratory, University of Cambridge, University of Florida, the French Participation Group, the German Participation Group, the Instituto de Astrofísica de Canarias, the Michigan State/Notre Dame/JINA Participation Group, Johns Hopkins University, Lawrence Berkeley National Laboratory, Max Planck Institute for Astrophysics, New Mexico State University, New York University, Ohio State University, Pennsylvania State University, University of Portsmouth, Princeton University, the Spanish Participation Group, University of Tokyo, University of Utah, Vanderbilt University, University of Virginia, University of Washington, and Yale University.

*Facilities:* Hiltner (OSMOS), Sloan, ARC (DIS), Du Pont (WFCCD).

## APPENDIX

### METALLICITY CONVERSIONS

It is well known that the various strong-line oxygen abundance estimators have different scales and zero-points. (For excellent pictorial representations of this, see Figure 2 of Kewley & Ellison (2008) or Figure 12 of Bresolin et al. (2009).) Because of these differences in scale and zero-point, it is critically necessary to put different estimates on a common scale before comparing abundances. Kewley & Ellison (2008) determined empirical conversions between many of the commonly used scales by fitting the trend defined by performing a given two diagnostics on a large sample of high S/N galaxy spectra from SDSS. While these conversions have been very useful to the community, there can be problems using them at very low metallicity. The forward and reverse conversions between two methods are not always consistent, or even monotonic, as can be seen by comparing the black solid and red dotted lines in Figure 14. The problem appears to be a consequence of the interaction between the vast statistical weight of the abundant high-metallicity galaxies and the third-order polynomials (the inversion of which cannot be precisely expressed as another

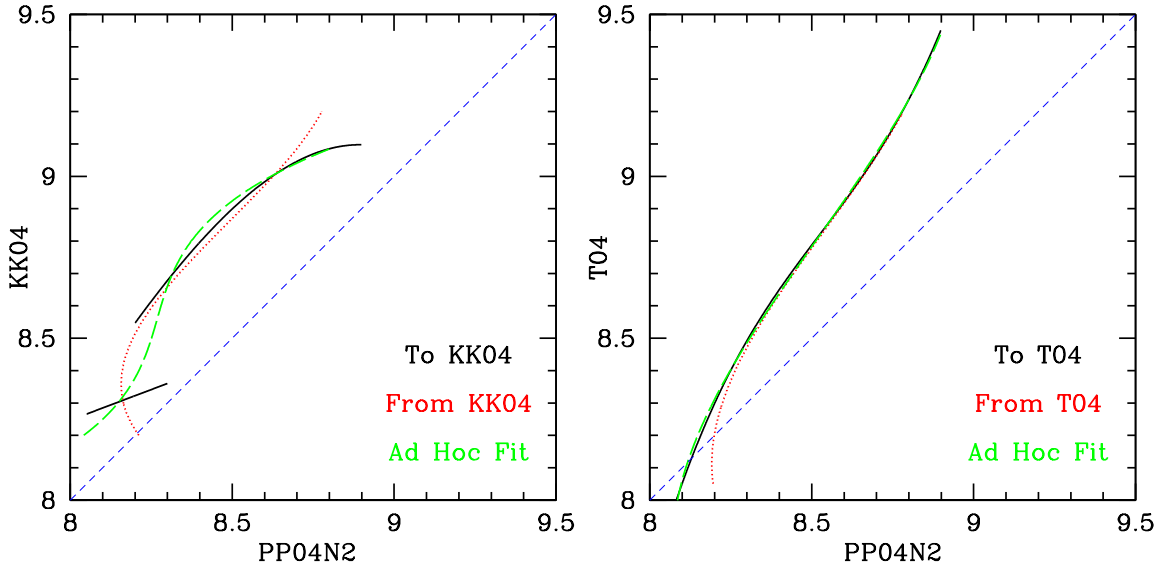


**Figure 14.** Forward and reverse conversion over the entire valid conversion ranges between the metallicity scale of Kobulnicky & Kewley (2004) and the N2 scale of Pettini & Pagel (2004) (left) and between Tremonti et al. (2004) and the N2 scale of Pettini & Pagel (2004) (right). To KK04 and T04 is the black solid line, while from KK04 and T04 is the red dotted line. The blue dashed line would represent a conversion between two exactly equivalent metallicity scales. The scales are the same as those in Figure 3 in Kewley & Ellison (2008). The green long-dashed lines show our fits to the forward conversions, which we use in Figure 10 to convert from KK04 and T04 to PP04N2 in order to ensure monotonic behavior at low metallicities.

third-order polynomial) in which the conversions are expressed. The high-metallicity end is tightly pinned, allowing low-metallicity end of the third-order polynomial to shift dramatically when the forward and reverse conversions are independently fit to the data.

Preserving monotonicity in a conversion is important when converting a continuous distribution, as can be dramatically seen in Figure 10. We are also concerned about the compounding errors involved in multiple conversions between different scales, which is perhaps the most problematic negative consequence of the difference between the forward and reverse conversions, in that even the simplest conversion chain (to another scale and back again) results in a different metallicity distribution. For applications involving more than one conversion, invertability can be more important than the extra precision from fitting the forward and reverse conversions independently to the data.

For the purposes of this paper, we need to avoid the double-value of the non-monotonic T04 to PP04N2 conversion at low metallicities in order to convert the metallicity distribution of star-formation. We do so by defining ad hoc conversions from T04 to PP04N2 and from KK04 to PP04N2, as shown in Figure 14. These conversion are third-order polynomial fits to the conversion from PP04N2 to T04 and from PP04N2 to KK04 given in Kewley & Ellison (2008). These fits are described by

$$y = a + bx + cx^2 + dx^3, \quad (\text{A1})$$

where  $y = 12 + \log(\text{O}/\text{H})_{\text{PP04N2}}$ . For T04,  $x = 12 + \log(\text{O}/\text{H})_{\text{T04}}$ ,  $a = 178.248$ ,  $b = -59.2077$ ,  $c = 6.80078$ , and  $d = -0.257326$ , and for KK04,  $x = 12 + \log(\text{O}/\text{H})_{\text{KK04}}$ ,  $a = -1657.85$ ,  $b = 583.307$ ,  $c = -68.1052$ , and  $d = 2.65189$ . Note that these are fits to fits rather than fits to data, and they are equivalent to mathematically inverting the conversion from PP04N2 to T04 or KK04 and approximating it as a third-order polynomial. We define them solely for the purposes of avoiding a double-valued function at low metallicity and matching the inverse conversion from PP04N2 to T04 and from PP04N2 to KK04.

#### REFERENCES

- Abazajian, K. N., et al. 2009, *ApJS*, 182, 543  
Aihara, H., et al. 2011, *ApJS*, 193, 29  
Anderson, J. P., Covarrubias, R. A., James, P. A., Hamuy, M., & Habergham, S. M. 2010, *MNRAS*, 407, 2660  
Anderson, J. P., Habergham, S. M., James, P. A., & Hamuy, M. 2012, *MNRAS*, 424, 1372  
Anderson, J. P., & James, P. A. 2008, *MNRAS*, 390, 1527  
Arcavi, I., et al. 2010, *ApJ*, 721, 777  
Asplund, M., Grevesse, N., Sauval, A. J., & Scott, P. 2009, *ARA&A*, 47, 481  
Assef, R. J., et al. 2008, *ApJ*, 676, 286  
Badenes, C., Harris, J., Zaritsky, D., & Prieto, J. L. 2009, *ApJ*, 700, 727  
Bell, E. F., McIntosh, D. H., Katz, N., & Weinberg, M. D. 2003, *ApJS*, 149, 289  
Bensby, T., Feltzing, S., & Lundström, I. 2004, *A&A*, 415, 155  
Berg, D. A., Skillman, E. D., & Marble, A. R. 2011, *ApJ*, 738, 2  
Bertin, E., & Arnouts, S. 1996, *A&AS*, 117, 393  
Blanton, M. R., Lin, H., Lupton, R. H., Maley, F. M., Young, N., Zehavi, I., & Loveday, J. 2003, *AJ*, 125, 2276  
Bresolin, F., Gieren, W., Kudritzki, R., Pietrzyński, G., Urbaneja, M. A., & Carraro, G. 2009, *ApJ*, 700, 309  
Brinchmann, J., Charlot, S., White, S. D. M., Tremonti, C., Kauffmann, G., Heckman, T., & Brinkmann, J. 2004, *MNRAS*, 351, 1151  
Bruzual, G., & Charlot, S. 2003, *MNRAS*, 344, 1000  
Campisi, M. A., Tapparello, C., Salvaterra, R., Mannucci, F., & Colpi, M. 2011, *MNRAS*, 417, 1013  
Chatzopoulos, E., et al. 2011, *ApJ*, 729, 143  
Chen, Y. Q., Zhao, G., Nissen, P. E., Bai, G. S., & Qiu, H. M. 2003, *ApJ*, 591, 925  
Chomiuk, L., et al. 2011, *ApJ*, 743, 114

- Cresci, G., Mannucci, F., Della Valle, M., & Maiolino, R. 2007, *A&A*, 462, 927
- Delahaye, F., & Pinsonneault, M. H. 2006, *ApJ*, 649, 529
- Denicoló, G., Terlevich, R., & Terlevich, E. 2002, *MNRAS*, 330, 69
- Eldridge, J. J., Izzard, R. G., & Tout, C. A. 2008, *MNRAS*, 384, 1109
- Epstein, C. R., Johnson, J. A., Dong, S., Udalski, A., Gould, A., & Becker, G. 2010, *ApJ*, 709, 447
- Fulbright, J. P., McWilliam, A., & Rich, R. M. 2007, *ApJ*, 661, 1152
- Georgy, C., Ekström, S., Meynet, G., Massey, P., Levesque, E. M., Hirschi, R., Eggenberger, P., & Maeder, A. 2012, *arXiv:1203.5243*
- Georgy, C., Meynet, G., Walder, R., Folini, D., & Maeder, A. 2009, *A&A*, 502, 611
- Gunn, J. E., et al. 2006, *AJ*, 131, 2332
- Han, X. H., Hammer, F., Liang, Y. C., Flores, H., Rodrigues, M., Hou, J. L., & Wei, J. Y. 2010, *A&A*, 514, A24
- Heger, A., & Woosley, S. E. 2002, *ApJ*, 567, 532
- Israelian, G., García López, R. J., & Rebolo, R. 1998, *ApJ*, 507, 805
- Jensen, A. G., & Snow, T. P. 2007, *ApJ*, 669, 378
- Johnson, J. A., Gal-Yam, A., Leonard, D. C., Simon, J. D., Udalski, A., & Gould, A. 2007, *ApJ*, 655, L33
- Kasen, D., & Woosley, S. E. 2009, *ApJ*, 703, 2205
- Kauffmann, G., et al. 2003, *MNRAS*, 341, 33
- Kelly, P. L., & Kirshner, R. P. 2012, *ApJ*, 759, 107
- Kelly, P. L., Kirshner, R. P., & Pahre, M. 2008, *ApJ*, 687, 1201
- Kessler, R., et al. 2009, *ApJS*, 185, 32
- Kewley, L. J., & Dopita, M. A. 2002, *ApJS*, 142, 35
- Kewley, L. J., & Ellison, S. L. 2008, *ApJ*, 681, 1183
- Kobulnicky, H. A., & Kewley, L. J. 2004, *ApJ*, 617, 240
- Kocevski, D., & West, A. A. 2011, *ApJ*, 735, L8
- Kozłowski, S., et al. 2010, *ApJ*, 722, 1624
- Kriek, M., van Dokkum, P. G., Labbé, I., Franx, M., Illingworth, G. D., Marchesini, D., & Quadri, R. F. 2009, *ApJ*, 700, 221
- Kudritzki, R., & Puls, J. 2000, *ARA&A*, 38, 613
- Langer, N., Norman, C. A., de Koter, A., Vink, J. S., Cantiello, M., & Yoon, S. 2007, *A&A*, 475, L19
- Lara-López, M. A., et al. 2010, *A&A*, 521, L53+
- Lecureur, A., Hill, V., Zoccali, M., Barbuy, B., Gómez, A., Minniti, D., Ortolani, S., & Renzini, A. 2007, *A&A*, 465, 799
- Leloudas, G., et al. 2011, *A&A*, 530, A95
- Levesque, E. M., Kewley, L. J., Berger, E., & Jabran Zahid, H. 2010, *AJ*, 140, 1557
- Li, W., et al. 2011, *MNRAS*, 412, 1441
- López-Sánchez, Á. R., Dopita, M. A., Kewley, L. J., Zahid, H. J., Nicholls, D. C., & Scharwächter, J. 2012, *MNRAS*, 426, 2630
- Maiolino, R., Vanzì, L., Mannucci, F., Cresci, G., Ghinassi, F., & Della Valle, M. 2002, *A&A*, 389, 84
- Mannucci, F., Cresci, G., Maiolino, R., Marconi, A., & Gnerucci, A. 2010, *MNRAS*, 408, 2115
- Mannucci, F., Salvaterra, R., & Campisi, M. A. 2011, *MNRAS*, 414, 1263
- Mannucci, F., et al. 2003, *A&A*, 401, 519
- Martini, P., et al. 2011, *PASP*, 123, 187
- McGaugh, S. S. 1991, *ApJ*, 380, 140
- McWilliam, A. 1997, *ARA&A*, 35, 503
- Modjaz, M., Filippenko, A. V., Silverman, J. M., Kleiser, I. K. W., & Morton, A. J. L. 2010, *The Astronomer's Telegram*, 2503, 1
- Modjaz, M., Kewley, L., Bloom, J. S., Filippenko, A. V., Perley, D., & Silverman, J. M. 2011, *ApJ*, 731, L4+
- Modjaz, M., et al. 2008, *AJ*, 135, 1136
- Murphy, J. W., Jennings, Z. G., Williams, B., Dalcanton, J. J., & Dolphin, A. E. 2011, *ApJ*, 742, L4
- Neill, J. D., et al. 2009, *ApJ*, 707, 1449
- . 2011, *ApJ*, 727, 15
- Niino, Y. 2011, *MNRAS*, 417, 567
- Ober, W. W., El Eid, M. F., & Fricke, K. J. 1983, *A&A*, 119, 61
- Okada, Y., Onaka, T., Miyata, T., Okamoto, Y. K., Sakon, I., Shibai, H., & Takahashi, H. 2008, *ApJ*, 682, 416
- Pagel, B. E. J., Edmunds, M. G., Blackwell, D. E., Chun, M. S., & Smith, G. 1979, *MNRAS*, 189, 95
- Pauldrach, A., Puls, J., & Kudritzki, R. P. 1986, *A&A*, 164, 86
- Pettini, M., & Pagel, B. E. J. 2004, *MNRAS*, 348, L59
- Prantzos, N., & Boissier, S. 2003, *A&A*, 406, 259
- Prieto, J., & Filippenko, A. V. 2010, *Central Bureau Electronic Telegrams*, 2224, 3
- Prieto, J. L., Stanek, K. Z., & Beacom, J. F. 2008, *ApJ*, 673, 999
- Rau, A., et al. 2009, *PASP*, 121, 1334
- Reddy, B. E., Lambert, D. L., & Allende Prieto, C. 2006, *MNRAS*, 367, 1329
- Reddy, B. E., Tomkin, J., Lambert, D. L., & Allende Prieto, C. 2003, *MNRAS*, 340, 304
- Rich, R. M., & Origlia, L. 2005, *ApJ*, 634, 1293
- Rich, R. M., Origlia, L., & Valenti, E. 2007, *ApJ*, 665, L119
- Rodríguez, M. 2002, *A&A*, 389, 556
- Salim, S., et al. 2007, *ApJS*, 173, 267
- Sanders, N. E., et al. 2012, *ApJ*, 756, 184
- Savaglio, S., et al. 2005, *ApJ*, 635, 260
- Smartt, S. J. 2009, *ARA&A*, 47, 63
- Stanek, K. Z., et al. 2006, *Acta Astron.*, 56, 333
- Stoll, R., Prieto, J. L., Stanek, K. Z., Pogge, R. W., Szczygiel, D. M., Pojmański, G., Antognini, J., & Yan, H. 2011, *ApJ*, 730, 34
- Stoll, R., et al. 2010, in *Proc. SPIE*, Vol. 7735, 154
- Tinsley, B. M. 1979, *ApJ*, 229, 1046
- Tremonti, C. A., et al. 2004, *ApJ*, 613, 898
- Uomoto, A., et al. 1999, in *Bulletin of the American Astronomical Society*, Vol. 31, American Astronomical Society Meeting Abstracts, 1501
- Vergani, S. D., et al. 2011, *A&A*, 535, A127
- Vink, J. S., & de Koter, A. 2005, *A&A*, 442, 587
- Wright, E. L. 2006, *PASP*, 118, 1711
- Yates, R. M., Kauffmann, G., & Guo, Q. 2012, *MNRAS*, 422, 215
- Yin, S. Y., Liang, Y. C., Hammer, F., Brinchmann, J., Zhang, B., Deng, L. C., & Flores, H. 2007, *A&A*, 462, 535
- York, D. G., et al. 2000, *AJ*, 120, 1579
- Young, D. R., et al. 2010, *A&A*, 512, A70
- Zaritsky, D., Kennicutt, Jr., R. C., & Huchra, J. P. 1994, *ApJ*, 420, 87

**Table 1**  
Observation properties

Telescope	Instrument	slit width (arcsec)	ruling (lines/mm)	$\lambda$ coverage ( $\text{\AA}$ )	resolution ( $\text{\AA}$ )
APO	DIS	1.5	B400/R300 (gratings)	3500–9800	7
du Pont	WFCCD	1.7	400 (blue grism)	3700–9200	7
Hiltner	OSMOS	1.2	704 (grism)	3960–6870	3
SDSS	fiber spectrograph	3 (dia)	B640/R440 (grisms)	3800–9200	3

**Table 2**  
Measured host metallicities

SN Name	z	type	H $\alpha$ $\lambda$ 6563 <sup>a</sup>	[N II] $\lambda$ 6584 <sup>a</sup>	12+log(O/H) (PP04N2)	[Fe/H] (8.86)	SN radius <sup>b</sup> (arcsec)	SN radius <sup>c</sup> (kpc)	Source
PTF09awk	0.0620	Ib	717 $\pm$ 3	126 $\pm$ 3	8.42 $\pm$ 0.03	-0.90	*0.10	0.11	SDSS
PTF09bce	0.0230	II	117 $\pm$ 3	45 $\pm$ 4	8.72 $\pm$ 0.10	-0.51	5.93	2.76	OSMOS
PTF09bcl	0.0620	II	117 $\pm$ 9	50 $\pm$ 8	8.77 $\pm$ 0.21	-0.45	... <sup>d</sup>	... <sup>d</sup>	APO
PTF09bgf	0.0310	II	643 $\pm$ 10	38 $\pm$ 11	8.18 $\pm$ 0.34	-1.19	1.17	0.72	duPont
PTF09cjg	0.0190	II	2982 $\pm$ 25	1107 $\pm$ 25	8.70 $\pm$ 0.03	-0.54	14.24	5.49	APO
PTF09cu	0.0570	II	60 $\pm$ 3	20 $\pm$ 3	8.66 $\pm$ 0.20	-0.59	9.14	10.10	APO
PTF09dah	0.0238	IIb	207 $\pm$ 4	31 $\pm$ 4	8.37 $\pm$ 0.15	-0.95	2.32	1.12	duPont
PTF09dfk	0.0160	Ib	601 $\pm$ 4	65 $\pm$ 4	8.30 $\pm$ 0.07	-1.05	1.25	0.41	duPont
PTF09dra	0.0770	II	145 $\pm$ 3	55 $\pm$ 3	8.72 $\pm$ 0.07	-0.52	*3.63	5.29	SDSS
PTF09due	0.0290	II	... <sup>e</sup>	... <sup>e</sup>	8.77 $\pm$ 0.05	-0.45	9.91	5.76	APOgrad
PTF09dxv	0.0330	IIb	277 $\pm$ 4	88 $\pm$ 4	8.63 $\pm$ 0.06	-0.63	6.26	4.12	duPont
PTF09ebq	0.0235	II	3304 $\pm$ 14	1175 $\pm$ 13	8.68 $\pm$ 0.01	-0.56	0.69	0.33	duPont
PTF09ecm	0.0285	II	149 $\pm$ 3	55 $\pm$ 4	8.70 $\pm$ 0.08	-0.54	5.17	2.96	duPont
PTF09fbf	0.0210	II	571 $\pm$ 3	85 $\pm$ 3	8.37 $\pm$ 0.04	-0.95	4.55	1.93	duPont
PTF09fma	0.0310	II	183 $\pm$ 5	57 $\pm$ 6	8.62 $\pm$ 0.13	-0.64	... <sup>d</sup>	... <sup>d</sup>	duPont
PTF09fmk	0.0631	II	451 $\pm$ 7	166 $\pm$ 8	8.70 $\pm$ 0.06	-0.54	3.68	4.47	duPont
PTF09fqa	0.0300	II	43 $\pm$ 1	7 $\pm$ 1	8.37 $\pm$ 0.22	-0.95	10.76	6.46	duPont
PTF09fsr	0.0079	Ib	296 $\pm$ 4	93 $\pm$ 4	8.63 $\pm$ 0.06	-0.63	64.61	10.55	duPont
PTF09g	0.0400	II	187 $\pm$ 3	62 $\pm$ 3	8.65 $\pm$ 0.06	-0.60	*3.83	3.03	SDSS
PTF09gof	0.1030	II	62 $\pm$ 3	17 $\pm$ 3	8.56 $\pm$ 0.20	-0.72	1.90	3.59	duPont
PTF09iex	0.0200	II	278 $\pm$ 7	18 $\pm$ 8	8.20 $\pm$ 0.56	-1.17	4.43	1.79	duPont
PTF09ige	0.0640	II	322 $\pm$ 2	97 $\pm$ 2	8.61 $\pm$ 0.02	-0.65	*5.10	6.28	SDSS
PTF09igz	0.0860	II	72 $\pm$ 3	18 $\pm$ 3	8.53 $\pm$ 0.19	-0.75	1.69	2.72	APO
PTF09ism	0.0290	II	100 $\pm$ 2	33 $\pm$ 2	8.65 $\pm$ 0.08	-0.61	*7.47	4.34	SDSS
PTF09jq	0.0900	Ic	201 $\pm$ 4	92 $\pm$ 4	8.81 $\pm$ 0.06	-0.40	*2.88	4.84	SDSS
PTF09r	0.0270	II	63 $\pm$ 3	22 $\pm$ 3	8.68 $\pm$ 0.18	-0.57	0.79	0.43	OSMOS
PTF09sh	0.0377	II	362 $\pm$ 9	90 $\pm$ 9	8.53 $\pm$ 0.12	-0.75	9.73	7.27	APO
PTF09sk	0.0355	Ic-BL	717 $\pm$ 3	73 $\pm$ 2	8.28 $\pm$ 0.04	-1.06	*2.77	1.95	SDSS
PTF09t	0.0390	II	775 $\pm$ 9	114 $\pm$ 9	8.37 $\pm$ 0.10	-0.96	5.84	4.51	duPont
PTF09tm	0.0350	II	232 $\pm$ 4	109 $\pm$ 4	8.83 $\pm$ 0.04	-0.38	*3.64	2.53	SDSS
PTF09uj	0.0651	II	85 $\pm$ 2	26 $\pm$ 2	8.61 $\pm$ 0.10	-0.65	*2.72	3.40	SDSS
PTF10bau	0.0260	II	... <sup>e</sup>	... <sup>e</sup>	8.73 $\pm$ 0.04	-0.50	6.18	3.23	grad
PTF10bgl	0.0300	II	... <sup>e</sup>	... <sup>e</sup>	8.63 $\pm$ 0.06	-0.63	8.19	4.92	OSMgrad
PTF10bhu	0.0360	Ic	152 $\pm$ 2	36 $\pm$ 2	8.51 $\pm$ 0.08	-0.78	*1.62	1.16	SDSS
PTF10bip	0.0510	Ic	229 $\pm$ 6	24 $\pm$ 5	8.29 $\pm$ 0.25	-1.05	1.24	1.23	duPont
PTF10con	0.0330	II	132 $\pm$ 5	44 $\pm$ 5	8.65 $\pm$ 0.14	-0.60	1.72	1.13	duPont
PTF10cqh	0.0410	II	318 $\pm$ 7	141 $\pm$ 7	8.80 $\pm$ 0.06	-0.42	9.17	7.43	duPont
PTF10cwx	0.0730	II	237 $\pm$ 4	31 $\pm$ 5	8.34 $\pm$ 0.19	-0.99	2.56	3.55	duPont
PTF10cxq	0.0470	II	286 $\pm$ 5	31 $\pm$ 5	8.30 $\pm$ 0.20	-1.05	1.53	1.41	duPont
PTF10cxx	0.0340	II	759 $\pm$ 4	326 $\pm$ 4	8.78 $\pm$ 0.02	-0.44	*1.84	1.24	SDSS
PTF10czn	0.0450	II	611 $\pm$ 13	132 $\pm$ 13	8.48 $\pm$ 0.12	-0.81	14.98	13.25	duPont
PTF10hv	0.0518	II	139 $\pm$ 2	35 $\pm$ 2	8.54 $\pm$ 0.06	-0.74	*5.59	5.65	SDSS
PTF10s	0.0510	II	271 $\pm$ 2	90 $\pm$ 2	8.65 $\pm$ 0.03	-0.60	*1.05	1.04	SDSS

<sup>a</sup>  $10^{-17}$  erg cm<sup>-2</sup> s<sup>-1</sup> Å<sup>-1</sup>

<sup>b</sup> SN radius from the center of the galaxy. Note that all targets are observed at the SN location or equivalent galactocentric radius except the 12 targets for which we use archival SDSS spectra (\*starred). For these 12 targets, the distance in this column is the distance between the SN location and the fiber center, which is half an arcsecond or less away from the center of the galaxy in all cases. Note that for these SDSS spectra, most SN locations are within the fiber diameter, and only one is more than 2 fiber diameters away.

<sup>c</sup> Projected physical radius calculated (Wright 2006) assuming  $H_0 = 70$ ,  $\Omega_m = 0.3$ , and  $\Omega_\Lambda = 0.7$ .

<sup>d</sup> PTF09bcl and PTF09fma are outside the SDSS photometry, so we do not determine the coordinates of their host galaxy centers.

<sup>e</sup> For PTF09due, PTF10bau, and PTF10bgl, the metallicity at the SN location is approximated by fitting a metallicity gradient to points at other galactocentric radii (see Table 3 for line fluxes and locations) and extrapolating or interpolating the metallicity at the radius of the SN.

**Table 3**  
Measured line fluxes and metallicities at non-supernova locations within the galaxy

SN Name	Source	Radius <sup>a</sup> (arcsec)	H $\alpha$ $\lambda$ 6563 <sup>b</sup>	[N II] $\lambda$ 6584 <sup>b</sup>	12+log(O/H) (PP04N2)
PTF09due	APO	13.0	276.0 $\pm$ 1.9	105.2 $\pm$ 2.0	8.72 $\pm$ 0.02
PTF09due	APO	25.0	202.2 $\pm$ 1.6	46.6 $\pm$ 1.5	8.51 $\pm$ 0.04
PTF10bau	SDSS	0.0	988.5 $\pm$ 6.9	379.5 $\pm$ 7.3	8.72 $\pm$ 0.02
PTF10bau	OSMOS	3.1	522.3 $\pm$ 1.8	209.8 $\pm$ 2.4	8.74 $\pm$ 0.01
PTF10bau	OSMOS	4.8	314.7 $\pm$ 2.1	124.8 $\pm$ 2.3	8.74 $\pm$ 0.02
PTF10bau	SDSS	10.5	565.2 $\pm$ 1.9	215.7 $\pm$ 2.0	8.72 $\pm$ 0.01
PTF10bau	OSMOS	10.6	122.8 $\pm$ 1.8	57.1 $\pm$ 1.9	8.82 $\pm$ 0.04
PTF10bau	OSMOS	12.9	152.7 $\pm$ 1.6	60.9 $\pm$ 1.6	8.74 $\pm$ 0.03
PTF10bau	OSMOS	19.8	35.9 $\pm$ 1.2	6.6 $\pm$ 0.7	8.43 $\pm$ 0.14
PTF10bgl	OSMOS	1.5	268.9 $\pm$ 4.4	107.7 $\pm$ 4.7	8.74 $\pm$ 0.06
PTF10bgl	OSMOS	5.9	164.3 $\pm$ 3.1	61.8 $\pm$ 3.4	8.71 $\pm$ 0.07
PTF10bgl	OSMOS	9.1	394.4 $\pm$ 2.9	116.3 $\pm$ 3.1	8.60 $\pm$ 0.03
PTF10bgl	OSMOS	13.7	851.3 $\pm$ 3.0	218.5 $\pm$ 3.2	8.54 $\pm$ 0.02
PTF10bgl	OSMOS	21.9	68.7 $\pm$ 2.6	21.8 $\pm$ 2.5	8.63 $\pm$ 0.14

<sup>a</sup> Galactocentric radius of the spectrum

<sup>b</sup>  $10^{-17}$  erg cm<sup>-2</sup> s<sup>-1</sup> Å<sup>-1</sup>

**Table 4**  
Host properties measured from SDSS photometry

SN (PTF)	Gal RA (J2000.0)	Gal Dec (J2000.0)	$f_u^a$ (Jy)	$f_g^a$ (Jy)	$f_r^a$ (Jy)	$f_i^a$ (Jy)	$f_z^a$ (Jy)
09aux	16:09:15.851	+29:17:37.09	1.42E-04±8.5E-06	5.87E-04±1.2E-05	1.15E-03±2.3E-05	1.57E-03±3.2E-05	1.99E-03±6.3E-05
09awk	13:37:56.354	+22:55:04.82	8.41E-05±5.4E-06	1.96E-04±4.2E-06	2.72E-04±5.8E-06	3.58E-04±7.9E-06	3.89E-04±1.6E-05
09axc	14:53:13.066	+22:14:32.22	2.51E-05±3.0E-06	9.85E-05±2.2E-06	1.88E-04±4.0E-06	2.40E-04±5.3E-06	2.78E-04±1.4E-05
09axi	14:12:40.942	+31:04:03.51	3.67E-05±6.1E-06	1.09E-04±2.9E-06	1.79E-04±4.9E-06	1.90E-04±6.4E-06	1.74E-04±1.9E-05
09bce	16:35:18.117	+55:38:03.60	1.02E-03±5.2E-05	4.05E-03±8.3E-05	8.23E-03±1.7E-04	1.20E-02±2.4E-04	1.55E-02±4.7E-04
09bgf	14:41:38.351	+19:21:43.21	5.69E-05±5.3E-06	1.29E-04±3.1E-06	1.65E-04±4.2E-06	1.89E-04±5.8E-06	2.08E-04±1.6E-05
09bw	15:05:02.037	+48:40:03.22	1.85E-06±1.8E-06	1.35E-05±1.1E-06	2.80E-05±1.5E-06	3.52E-05±2.5E-06	3.54E-05±7.6E-06
09cjq	21:16:27.580	-00:49:35.16	2.97E-03±1.5E-04	1.05E-02±2.1E-04	2.10E-02±4.2E-04	2.96E-02±6.0E-04	3.93E-02±1.2E-03
09ct	11:42:13.837	+10:38:53.86	1.03E-05±2.5E-06	2.68E-05±1.2E-06	5.51E-05±2.2E-06	7.46E-05±3.5E-06	9.48E-05±1.1E-05
09cu	13:15:23.892	+46:25:13.40	3.85E-04±2.0E-05	1.05E-03±2.2E-05	1.77E-03±3.6E-05	2.38E-03±4.9E-05	2.83E-03±9.3E-05
09cvi	21:47:09.984	+08:18:35.58	-1.11E-06±1.2E-06	4.06E-06±4.3E-07	4.63E-06±6.9E-07	4.97E-06±1.1E-06	9.74E-06±3.9E-06
09dah	22:45:17.115	+21:49:17.34	1.80E-04±1.3E-05	3.79E-04±8.2E-06	5.11E-04±1.2E-05	6.63E-04±1.6E-05	7.64E-04±4.0E-05
09dfk	23:09:13.471	+07:48:16.39	1.28E-04±7.9E-06	3.53E-04±7.5E-06	5.40E-04±1.1E-05	6.87E-04±1.5E-05	8.28E-04±3.2E-05
09djl	16:33:55.969	+30:14:16.65	4.05E-06±2.1E-06	1.76E-05±8.0E-07	4.63E-05±1.4E-06	5.80E-05±2.2E-06	8.44E-05±9.8E-06
09dra	15:48:11.297	+41:13:31.76	2.40E-04±1.5E-05	5.98E-04±1.3E-05	9.95E-04±2.1E-05	1.34E-03±2.9E-05	1.63E-03±5.9E-05
09due	16:26:53.240	+51:33:18.35	2.35E-03±1.2E-04	6.12E-03±1.3E-04	9.42E-03±1.9E-04	1.17E-02±2.4E-04	1.41E-02±4.3E-04
09dxv	23:08:34.828	+18:56:19.80	3.99E-04±2.6E-05	1.17E-03±2.4E-05	1.94E-03±4.0E-05	2.77E-03±5.9E-05	3.55E-03±1.3E-04
09dzt	16:03:03.823	+21:01:47.28	9.55E-05±9.2E-06	2.00E-04±4.9E-06	3.32E-04±8.7E-06	4.26E-04±1.3E-05	5.39E-04±4.2E-05
09ebq	00:14:01.743	+29:25:58.47	5.79E-04±2.9E-05	1.44E-03±2.9E-05	2.40E-03±4.8E-05	3.15E-03±6.5E-05	4.01E-03±1.3E-04
09ecm	01:06:43.123	-06:22:46.04	3.60E-04±2.4E-05	1.08E-03±2.3E-05	1.83E-03±3.8E-05	2.26E-03±4.8E-05	2.86E-03±1.0E-04
09ejz	00:55:07.230	-06:57:04.82	5.63E-05±8.0E-06	1.86E-04±4.4E-06	4.32E-04±9.5E-06	6.28E-04±1.4E-05	8.24E-04±3.4E-05
09faf	17:26:20.127	+72:56:28.74	2.23E-05±3.3E-06	3.59E-05±1.3E-06	3.76E-05±1.9E-06	4.74E-05±2.9E-06	8.00E-05±1.1E-05
09fbf	21:20:38.208	+01:02:49.97	1.59E-03±8.1E-05	4.36E-03±9.0E-05	6.76E-03±1.4E-04	8.65E-03±1.8E-04	1.06E-02±3.3E-04
09fmk	23:57:46.435	+11:58:44.53	1.65E-04±1.3E-05	4.44E-04±9.6E-06	7.74E-04±1.7E-05	1.21E-03±2.7E-05	1.40E-03±6.1E-05
09foy	23:17:10.983	+17:15:04.12	1.99E-04±1.5E-05	5.79E-04±1.2E-05	9.82E-04±2.1E-05	1.34E-03±2.9E-05	1.50E-03±6.9E-05
09fqa	22:25:33.064	+18:59:44.12	4.48E-04±2.7E-05	1.30E-03±2.7E-05	2.11E-03±4.4E-05	2.71E-03±5.7E-05	3.16E-03±1.1E-04
09fsr	23:04:56.569	+12:19:21.47	1.61E-02±7.8E-04	6.23E-02±1.3E-03	1.24E-01±2.5E-03	1.73E-01±3.5E-03	2.13E-01±6.5E-03
09g	15:16:31.418	+54:27:31.04	4.12E-04±2.1E-05	9.85E-04±2.0E-05	1.40E-03±2.9E-05	1.66E-03±3.4E-05	1.87E-03±6.7E-05
09gof	01:22:25.476	+03:38:08.80	7.57E-05±8.2E-06	1.91E-04±4.5E-06	3.21E-04±7.5E-06	3.74E-04±1.0E-05	4.07E-04±2.8E-05
09gtt	02:20:37.291	+02:24:24.30	4.74E-05±9.5E-06	1.39E-04±4.0E-06	1.78E-04±5.9E-06	2.73E-04±9.8E-06	2.85E-04±4.0E-05
09hdo	00:15:22.815	+30:43:16.29	4.55E-04±2.4E-05	1.59E-03±3.3E-05	3.17E-03±6.4E-05	4.60E-03±9.4E-05	6.01E-03±1.9E-04
09hgz	11:50:56.789	+21:11:50.06	3.64E-04±2.1E-05	1.38E-03±2.9E-05	2.97E-03±6.0E-05	4.45E-03±9.1E-05	6.25E-03±1.9E-04
09iex	12:02:46.955	+02:24:02.61	8.43E-05±9.2E-06	1.59E-04±4.6E-06	1.94E-04±6.7E-06	2.28E-04±1.0E-05	3.01E-04±3.9E-05
09ige	08:55:34.126	+32:40:01.34	1.39E-04±8.1E-06	3.49E-04±7.4E-06	4.98E-04±1.1E-05	6.26E-04±1.4E-05	6.35E-04±2.7E-05
09igz	08:53:56.582	+33:40:10.68	3.04E-05±4.1E-06	7.07E-05±2.0E-06	1.04E-04±3.4E-06	1.29E-04±5.0E-06	1.42E-04±1.6E-05
09ism	11:44:35.370	+10:12:46.55	1.98E-04±1.5E-05	4.85E-04±1.1E-05	7.06E-04±1.6E-05	8.73E-04±2.2E-05	9.28E-04±6.2E-05
09ps	16:14:08.619	+55:41:41.78	2.18E-05±3.0E-06	4.35E-05±1.2E-06	6.19E-05±1.8E-06	7.92E-05±2.6E-06	6.72E-05±1.1E-05
09q	12:24:50.022	+08:26:01.27	1.49E-04±1.1E-05	4.47E-04±9.6E-06	8.69E-04±1.8E-05	1.24E-03±2.6E-05	1.51E-03±5.2E-05
09r	14:18:58.607	+35:23:15.26	4.01E-05±4.0E-06	1.37E-04±3.1E-06	2.54E-04±5.5E-06	3.32E-04±7.6E-06	3.98E-04±1.9E-05
09sh	16:13:58.581	+39:31:50.29	6.53E-04±3.6E-05	1.46E-03±3.0E-05	2.34E-03±4.8E-05	3.04E-03±6.4E-05	2.83E-03±1.2E-04
09sk	13:30:51.179	+30:20:02.22	1.15E-04±6.7E-06	2.52E-04±5.6E-06	3.19E-04±6.9E-06	3.87E-04±9.1E-06	4.14E-04±1.9E-05
09t	14:15:42.905	+16:12:00.93	5.39E-04±2.8E-05	1.24E-03±2.5E-05	1.67E-03±3.4E-05	1.99E-03±4.2E-05	2.14E-03±7.8E-05
09tm	13:46:55.509	+61:33:17.33	4.21E-04±2.1E-05	1.41E-03±2.9E-05	2.68E-03±5.4E-05	3.76E-03±7.7E-05	4.84E-03±1.5E-04
09uj	14:20:10.883	+53:33:42.11	1.14E-04±8.0E-06	2.86E-04±6.3E-06	4.33E-04±9.5E-06	5.28E-04±1.2E-05	5.38E-04±2.8E-05
10bau	09:16:21.696	+17:43:38.08	2.47E-03±1.2E-04	6.20E-03±1.3E-04	1.02E-02±2.0E-04	1.28E-02±2.6E-04	1.56E-02±4.8E-04
10bfz	12:54:41.278	+15:24:16.42	1.80E-06±1.1E-06	4.07E-06±4.7E-07	6.37E-06±7.6E-07	4.20E-06±1.4E-06	1.20E-06±5.1E-06
10bgl	10:19:05.166	+46:27:16.67	3.40E-03±1.6E-04	8.80E-03±1.8E-04	1.27E-02±2.6E-04	1.57E-02±3.2E-04	1.77E-02±5.4E-04
10bhu	12:55:28.353	+53:34:30.63	2.17E-04±1.3E-05	5.53E-04±1.2E-05	8.10E-04±1.7E-05	9.83E-04±2.2E-05	1.17E-03±4.5E-05
10bip	12:34:10.493	+08:21:49.67	2.75E-05±3.5E-06	9.00E-05±2.2E-06	1.16E-04±3.0E-06	1.46E-04±4.1E-06	1.74E-04±1.2E-05
10bzf	11:44:02.964	+55:41:22.55	3.89E-05±4.7E-06	5.33E-05±1.1E-06	8.66E-05±3.0E-06	1.09E-04±4.5E-06	1.37E-04±1.6E-05
10cd	03:00:33.086	+36:15:25.02	2.11E-05±5.1E-06	5.21E-05±2.1E-06	9.28E-05±3.7E-06	8.22E-05±5.4E-06	1.02E-04±1.9E-05
10con	16:11:39.154	+00:52:31.87	2.36E-04±2.2E-05	6.06E-04±1.4E-05	1.61E-03±3.5E-05	3.58E-03±7.5E-05	2.85E-03±1.1E-04
10cqh	16:10:36.992	-01:43:01.65	5.53E-04±2.9E-05	1.98E-03±4.1E-05	3.91E-03±7.9E-05	5.67E-03±1.2E-04	7.45E-03±2.3E-04
10cwx	12:33:16.405	-00:03:12.34	4.72E-05±4.0E-06	9.72E-05±2.6E-06	1.23E-04±3.7E-06	1.60E-04±5.3E-06	1.73E-04±1.7E-05
10cxq	13:48:19.317	+13:28:57.27	1.03E-04±6.6E-06	2.23E-04±4.9E-06	2.77E-04±6.4E-06	3.22E-04±8.3E-06	3.25E-04±2.1E-05
10cxx	14:47:27.701	+01:55:05.28	7.97E-04±1.5E-05	9.62E-04±2.0E-05	1.81E-03±3.7E-05	2.48E-03±5.1E-05	3.31E-03±1.1E-04
10czn	14:51:17.242	+15:26:46.79	8.36E-04±4.4E-05	2.63E-03±5.4E-05	4.19E-03±8.5E-05	5.38E-03±1.1E-04	6.08E-03±2.0E-04
10dk	05:08:21.597	+00:12:42.28	1.11E-06±2.0E-06	5.16E-06±6.5E-07	9.23E-06±1.1E-06	9.73E-06±1.7E-06	9.92E-06±7.6E-06
10dvv	17:16:10.672	+31:47:32.32	1.81E-03±8.8E-05	4.49E-03±9.2E-05	7.00E-03±1.4E-04	8.64E-03±1.8E-04	1.06E-02±3.2E-04
10hvv	14:03:56.535	+54:27:27.21	1.51E-04±1.0E-05	4.23E-04±9.2E-06	5.92E-04±1.3E-05	7.55E-04±1.7E-05	8.11E-04±3.7E-05
10iin	07:50:00.984	+33:06:27.99	2.64E-06±1.8E-06	7.66E-06±7.3E-07	9.70E-06±1.3E-06	1.63E-05±1.8E-06	1.16E-05±6.3E-06
10s	10:37:16.292	+38:06:23.57	8.95E-05±6.5E-06	2.37E-04±5.1E-06	3.67E-04±7.9E-06	4.55E-04±1.0E-05	5.21E-04±2.1E-05
10ts	12:33:55.888	+13:55:08.31	1.70E-04±1.0E-05	4.53E-04±9.9E-06	7.26E-04±1.5E-05	9.44E-04±2.1E-05	1.06E-03±4.8E-05
10u	10:09:58.780	+46:00:33.68	6.48E-07±1.1E-06	1.62E-06±4.8E-07	6.87E-06±7.7E-07	9.58E-06±1.3E-06	1.43E-05±4.4E-06

<sup>a</sup>  $3\sigma$  upper limits for the fluxes of PTF09be and PTF09gyp are calculated as  $3\sigma_{\text{sky}}\sqrt{\pi r^2}$ , where  $r$  is set to 5 kpc (projected) at the distance of the supernova.

**Table 5**  
Host properties derived from SDSS photometry

SN (PTF)	type	SN RA (J2000.0)	SN Dec (J2000.0)	$z$	$\mu^a$	$M_u^b$	$M_g^b$	$M_r^b$	$M_i^b$	$M_z^b$	$M_B^b$
09aux	Ic/Ia	16:09:15.84	+29:17:36.7	0.047	36.60	-18.43	-19.85	-20.49	-20.79	-21.03	-19.48
09awk	Ib	13:37:56.36	+22:55:04.8	0.062	37.22	-18.37	-19.18	-19.50	-19.72	-19.84	-18.90
09axc	II	14:53:13.06	+22:14:32.2	0.115	38.64	-18.70	-20.07	-20.59	-20.80	-20.94	-19.75
09axi	II	14:12:40.82	+31:04:03.3	0.064	37.29	-17.55	-18.60	-19.07	-19.11	-19.02	-18.35
09bce	II	16:35:17.66	+55:37:59.1	0.023	35.01	-18.76	-20.22	-20.95	-21.34	-21.62	-19.85
09bgf	II	14:41:38.28	+19:21:43.8	0.031	35.67	-16.39	-17.15	-17.38	-17.50	-17.59	-16.91
09bw	II	15:05:02.04	+48:40:01.9	0.150	39.27	-16.47	-18.58	-19.11	-19.32	-19.32	-18.25
09cjq	II	21:16:28.48	-00:49:39.7	0.019	34.58	-19.76	-21.03	-21.70	-22.01	-22.29	-20.67
09ct	II	11:42:13.80	+10:38:53.9	0.150	39.27	-18.35	-19.38	-19.90	-20.17	-20.42	-19.07
09cu	II	13:15:23.14	+46:25:08.6	0.057	37.03	-19.80	-20.82	-21.33	-21.61	-21.81	-20.51
09cvi	II	21:47:09.80	+08:18:35.6	0.030	35.59	99.99	-13.51	-13.56	-13.58	-14.27	-13.18
09dah	IIb	22:45:17.05	+21:49:15.2	0.024	35.08	-17.17	-17.85	-18.12	-18.35	-18.48	-17.60
09dfk	Ib	23:09:13.42	+07:48:15.4	0.016	34.21	-15.90	-16.89	-17.29	-17.51	-17.68	-16.60
09djl	II	16:33:55.94	+30:14:16.3	0.184	39.75	-17.92	-19.52	-20.20	-20.39	-20.79	-19.20
09dra	II	15:48:11.47	+41:13:28.2	0.077	37.71	-19.98	-20.93	-21.41	-21.68	-21.91	-20.63
09due	II	16:26:52.36	+51:33:23.9	0.029	35.52	-20.23	-21.18	-21.62	-21.83	-22.03	-20.90
09dxv	IIb	23:08:34.73	+18:56:13.7	0.033	35.81	-19.38	-20.24	-20.61	-20.86	-21.04	-19.97
09dzt	Ic	16:03:04.20	+21:01:47.2	0.087	38.00	-19.62	-20.30	-20.72	-20.85	-21.09	-20.05
09ebq	II	00:14:01.69	+29:25:58.5	0.024	35.05	-18.32	-19.23	-19.74	-19.99	-20.23	-18.93
09ecm	II	01:06:43.16	-06:22:40.9	0.029	35.48	-18.82	-19.74	-20.15	-20.27	-20.45	-19.47
09ejz	Ic/Ia	00:55:07.29	-06:57:05.4	0.110	38.54	-19.72	-20.92	-21.59	-21.88	-22.13	-20.57
09fae	IIb	17:26:20.33	+72:56:30.6	0.067	37.40	-17.07	-17.52	-17.59	-17.68	-18.29	-17.29
09fbf	II	21:20:38.44	+01:02:52.9	0.021	34.80	-19.36	-20.30	-20.69	-20.90	-21.08	-20.02
09fmk	II	23:57:46.19	+11:58:45.3	0.063	37.26	-19.49	-20.40	-20.95	-21.24	-21.41	-20.08
09foy	II	23:17:10.58	+17:15:03.2	0.060	37.15	-19.39	-20.41	-20.89	-21.16	-21.28	-20.11
09fqa	II	22:25:32.33	+18:59:41.4	0.030	35.59	-18.66	-19.69	-20.15	-20.38	-20.52	-19.39
09fsr	Ib	23:04:52.98	+12:19:59.0	0.008	32.67	-19.89	-21.19	-21.81	-22.09	-22.25	-20.84
09g	II	15:16:31.48	+54:27:34.7	0.040	36.23	-19.07	-19.90	-20.25	-20.41	-20.54	-19.65
09gof	II	01:22:25.60	+03:38:08.4	0.103	38.38	-19.56	-20.43	-20.85	-20.97	-21.06	-20.18
09gtt	II	02:20:37.70	+02:24:13.2	0.041	36.29	-16.92	-17.92	-18.14	-18.56	-18.59	-17.62
09hdo	II	00:15:23.20	+30:43:19.3	0.047	36.60	-19.83	-21.06	-21.69	-22.02	-22.29	-20.71
09hgz	II	11:50:57.74	+21:11:49.4	0.028	35.44	-18.21	-19.62	-20.37	-20.77	-21.12	-19.25
09iex	II	12:02:46.86	+02:24:06.8	0.020	34.70	-15.79	-16.40	-16.60	-16.74	-17.03	-16.16
09ige	II	08:55:34.24	+32:39:57.0	0.064	37.29	-19.07	-19.91	-20.22	-20.43	-20.44	-19.66
09igz	II	08:53:56.70	+33:40:11.5	0.086	37.97	-18.09	-18.89	-19.21	-19.38	-19.49	-18.63
09ism	II	11:44:35.87	+10:12:43.7	0.029	35.52	-17.82	-18.62	-18.95	-19.12	-19.15	-18.37
09ps	Ic	16:14:08.62	+55:41:41.4	0.106	38.46	-18.09	-18.79	-19.11	-19.25	-19.14	-18.54
09q	Ic	12:24:50.11	+08:25:58.8	0.090	38.07	-19.92	-21.07	-21.67	-21.98	-22.21	-20.73
09r	II	14:18:58.63	+35:23:16.0	0.027	35.36	-15.63	-16.90	-17.53	-17.80	-18.00	-16.57
09sh	II	16:13:58.08	+39:31:58.1	0.038	36.10	-19.36	-20.18	-20.68	-20.92	-20.86	-19.92
09sk	Ic-BL	13:30:51.15	+30:20:04.9	0.035	35.97	-17.38	-18.13	-18.36	-18.55	-18.62	-17.88
09t	II	14:15:43.29	+16:11:59.1	0.039	36.18	-19.30	-20.08	-20.38	-20.54	-20.63	-19.84
09tm	II	13:46:55.94	+61:33:15.6	0.035	35.94	-18.78	-20.05	-20.69	-21.03	-21.30	-19.69
09uj	II	14:20:11.15	+53:33:41.0	0.065	37.33	-18.80	-19.68	-20.07	-20.25	-20.28	-19.42
10bau	II	09:16:21.29	+17:43:40.2	0.026	35.28	-20.08	-21.00	-21.50	-21.71	-21.92	-20.71
10bfz	Ic-BL	12:54:41.27	+15:24:17.0	0.150	39.27	-16.29	-17.09	-17.34	-16.87	-15.52	-16.82
10bgl	II	10:19:04.70	+46:27:23.3	0.030	35.59	-20.67	-21.62	-22.00	-22.20	-22.33	-21.34
10bhu	Ic	12:55:28.44	+53:34:28.7	0.036	36.00	-18.12	-19.03	-19.42	-19.60	-19.79	-18.75
10bip	Ic	12:34:10.52	+08:21:48.5	0.051	36.78	-16.72	-17.87	-18.10	-18.32	-18.51	-17.56
10bzf	Ic-BL	11:44:02.99	+55:41:27.6	0.050	36.73	-16.81	-17.21	-17.77	-17.94	-18.22	-16.97
10cd	II	03:00:32.93	+36:15:25.4	0.045	36.52	-17.11	-17.71	-18.13	-17.81	-17.94	-17.51
10con	II	16:11:39.09	+00:52:33.3	0.033	35.81	-18.55	-19.41	-20.35	-21.07	-20.77	-19.08
10cqj	II	16:10:37.60	-01:43:00.7	0.041	36.29	-20.13	-21.25	-21.81	-22.09	-22.31	-20.93
10cwx	II	12:33:16.53	-00:03:10.6	0.073	37.59	-18.12	-18.79	-19.05	-19.18	-19.32	-18.53
10cxq	II	13:48:19.32	+13:28:58.8	0.047	36.60	-17.96	-18.67	-18.86	-18.98	-18.99	-18.43
10cxx	II	14:47:27.78	+01:55:03.8	0.034	35.87	-18.40	-19.65	-20.26	-20.56	-20.86	-19.30
10czn	II	14:51:16.23	+15:26:43.6	0.045	36.50	-20.23	-21.33	-21.78	-22.00	-22.13	-21.02
10dk	II	05:08:21.54	+00:12:42.9	0.074	37.62	-14.43	-15.89	-16.37	-16.35	-16.34	-15.63
10dvb	II	17:16:12.25	+31:47:36.0	0.023	35.00	-19.50	-20.40	-20.83	-21.02	-21.22	-20.11
10hvv	II	14:03:56.18	+54:27:31.1	0.052	36.81	-18.56	-19.56	-19.88	-20.12	-20.21	-19.27
10in	IIb	07:50:01.24	+33:06:23.8	0.070	37.50	-15.08	-16.08	-16.27	-16.73	-16.36	-15.80
10s	II	10:37:16.30	+38:06:23.2	0.051	36.78	-18.00	-18.94	-19.36	-19.56	-19.71	-18.66
10ts	II	12:33:56.40	+13:55:08.3	0.046	36.55	-18.52	-19.47	-19.92	-20.16	-20.28	-19.18
10u	II	10:09:58.42	+46:00:35.2	0.150	39.27	-15.69	-16.48	-17.68	-17.96	-18.38	-16.38

<sup>a</sup> Assuming  $H_0 = 70$ ,  $\Omega_m = 0.3$ , and  $\Omega_\Lambda = 0.7$

<sup>b</sup> Magnitudes are corrected for galactic extinction but not intrinsic extinction.

**Table 6**  
Host galaxy properties fit from SDSS photometry

SN Name	type	M log M <sub>⊙</sub>	SFR (FAST) log M <sub>⊙</sub> /yr	SFR (u) log M <sub>⊙</sub> /yr	SSFR log yr <sup>-1</sup>	Age log yr
PTF09aux	Ic/Ia	10.43 <sup>+0.03</sup> <sub>-0.07</sub>	-0.59 <sup>+0.43</sup> <sub>-0.00</sub>	-0.06	-11.03 <sup>+0.45</sup> <sub>-0.00</sub>	9.70 <sup>+0.02</sup> <sub>-0.16</sub>
PTF09awk	Ib	9.45 <sup>+0.18</sup> <sub>-0.14</sub>	0.61 <sup>+0.35</sup> <sub>-0.73</sub>	0.44	-8.85 <sup>+0.47</sup> <sub>-0.83</sub>	8.80 <sup>+0.56</sup> <sub>-0.42</sub>
PTF09axc	II	10.33 <sup>+0.01</sup> <sub>-0.09</sub>	-0.25 <sup>+0.33</sup> <sub>-0.00</sub>	0.04	-10.58 <sup>+0.36</sup> <sub>-0.00</sub>	9.60 <sup>+0.01</sup> <sub>-0.11</sub>
PTF09axi	II	9.35 <sup>+0.09</sup> <sub>-0.04</sub>	-0.33 <sup>+0.03</sup> <sub>-0.16</sub>	-0.31	-9.68 <sup>+0.00</sup> <sub>-0.24</sub>	9.30 <sup>+0.06</sup> <sub>-0.20</sub>
PTF09bce	II	10.68 <sup>+0.08</sup> <sub>-0.09</sub>	0.11 <sup>+0.83</sup> <sub>-0.95</sub>	0.36	-10.58 <sup>+0.90</sup> <sub>-1.01</sub>	9.60 <sup>+0.20</sup> <sub>-0.37</sub>
PTF09bgf	II	8.59 <sup>+0.06</sup> <sub>-0.19</sub>	-0.88 <sup>+0.74</sup> <sub>-0.00</sub>	-0.80	-9.47 <sup>+0.87</sup> <sub>-0.00</sub>	9.20 <sup>+0.06</sup> <sub>-0.68</sub>
PTF09bw	II	9.75 <sup>+0.02</sup> <sub>-0.15</sub>	-0.83 <sup>+0.34</sup> <sub>-0.00</sub>	-0.77	-10.58 <sup>+0.36</sup> <sub>-0.00</sub>	9.60 <sup>+0.02</sup> <sub>-0.19</sub>
PTF09cjq	II	10.84 <sup>+0.05</sup> <sub>-0.14</sub>	0.62 <sup>+0.98</sup> <sub>-0.37</sub>	0.71	-10.22 <sup>+1.09</sup> <sub>-0.36</sub>	9.50 <sup>+0.15</sup> <sub>-0.52</sub>
PTF09ct	II	10.00 <sup>+0.10</sup> <sub>-0.19</sub>	-0.22 <sup>+1.46</sup> <sub>-0.27</sub>	-0.00	-10.22 <sup>+1.62</sup> <sub>-0.36</sub>	9.50 <sup>+0.10</sup> <sub>-0.95</sub>
PTF09cu	II	10.48 <sup>+0.09</sup> <sub>-0.19</sub>	0.81 <sup>+0.89</sup> <sub>-0.51</sub>	0.77	-9.68 <sup>+1.08</sup> <sub>-0.54</sub>	9.30 <sup>+0.22</sup> <sub>-0.71</sub>
PTF09cvi	II	7.07 <sup>+0.17</sup> <sub>-0.15</sub>	< -2.06 <sup>+0.38</sup> <sub>-0.42</sub>	-1.63	-9.13 <sup>+0.41</sup> <sub>-0.55</sub>	9.00 <sup>+0.34</sup> <sub>-0.34</sub>
PTF09dah	IIB	8.50 <sup>+0.38</sup> <sub>-0.13</sub>	1.70 <sup>+0.02</sup> <sub>-1.72</sub>	0.83	-6.80 <sup>+0.00</sup> <sub>-2.05</sub>	6.80 <sup>+2.10</sup> <sub>-0.08</sub>
PTF09dfk	Ib	8.77 <sup>+0.07</sup> <sub>-0.14</sub>	-0.91 <sup>+0.24</sup> <sub>-0.72</sub>	-0.80	-9.68 <sup>+0.83</sup> <sub>-0.24</sub>	9.30 <sup>+0.13</sup> <sub>-0.10</sub>
PTF09djl	II	10.22 <sup>+0.09</sup> <sub>-0.06</sub>	-0.35 <sup>+0.06</sup> <sub>-0.36</sub>	-0.16	-10.58 <sup>+0.00</sup> <sub>-0.45</sub>	9.60 <sup>+0.10</sup> <sub>-0.09</sub>
PTF09dra	II	10.34 <sup>+0.22</sup> <sub>-0.14</sub>	1.62 <sup>+0.32</sup> <sub>-1.28</sub>	1.33	-8.72 <sup>+0.45</sup> <sub>-1.50</sub>	8.70 <sup>+0.80</sup> <sub>-0.41</sub>
PTF09due	II	10.51 <sup>+0.07</sup> <sub>-0.18</sub>	0.83 <sup>+0.82</sup> <sub>-0.25</sub>	0.79	-9.68 <sup>+0.96</sup> <sub>-0.24</sub>	9.30 <sup>+0.14</sup> <sub>-0.64</sub>
PTF09dxv	IIB	9.93 <sup>+0.19</sup> <sub>-0.11</sub>	1.20 <sup>+0.26</sup> <sub>-1.01</sub>	0.95	-8.72 <sup>+0.34</sup> <sub>-1.20</sub>	8.70 <sup>+0.70</sup> <sub>-0.31</sub>
PTF09dzt	Ic	9.48 <sup>+0.36</sup> <sub>-0.10</sub>	2.58 <sup>+0.13</sup> <sub>-1.24</sub>	1.70	-6.89 <sup>+0.09</sup> <sub>-1.60</sub>	6.90 <sup>+1.61</sup> <sub>-0.12</sub>
PTF09ebq	II	9.59 <sup>+0.24</sup> <sub>-0.15</sub>	0.99 <sup>+0.30</sup> <sub>-1.11</sub>	0.74	-8.60 <sup>+0.43</sup> <sub>-1.32</sub>	8.60 <sup>+0.81</sup> <sub>-0.41</sub>
PTF09ecm	II	9.83 <sup>+0.06</sup> <sub>-0.09</sub>	0.15 <sup>+0.50</sup> <sub>-0.19</sub>	0.18	-9.68 <sup>+0.55</sup> <sub>-0.24</sub>	9.30 <sup>+0.11</sup> <sub>-0.36</sub>
PTF09ejz	Ic/Ia	10.79 <sup>+0.05</sup> <sub>-0.08</sub>	0.22 <sup>+0.85</sup> <sub>-0.06</sub>	0.50	-10.58 <sup>+0.90</sup> <sub>-0.00</sub>	9.60 <sup>+0.05</sup> <sub>-0.33</sub>
PTF09fae	IIB	8.03 <sup>+0.23</sup> <sub>-0.13</sub>	0.56 <sup>+0.33</sup> <sub>-0.41</sub>	0.06	-7.47 <sup>+0.38</sup> <sub>-0.59</sub>	7.50 <sup>+0.63</sup> <sub>-0.42</sub>
PTF09fbf	II	10.08 <sup>+0.10</sup> <sub>-0.13</sub>	0.61 <sup>+0.63</sup> <sub>-0.40</sub>	0.54	-9.47 <sup>+0.75</sup> <sub>-0.43</sub>	9.20 <sup>+0.22</sup> <sub>-0.51</sub>
PTF09fmk	II	10.12 <sup>+0.23</sup> <sub>-0.16</sub>	1.52 <sup>+0.31</sup> <sub>-1.14</sub>	1.22	-8.60 <sup>+0.43</sup> <sub>-1.32</sub>	8.60 <sup>+0.84</sup> <sub>-0.44</sub>
PTF09foy	II	10.30 <sup>+0.07</sup> <sub>-0.11</sub>	0.38 <sup>+0.70</sup> <sub>-0.26</sub>	0.44	-9.92 <sup>+0.79</sup> <sub>-0.30</sub>	9.40 <sup>+0.11</sup> <sub>-0.40</sub>
PTF09fqa	II	9.97 <sup>+0.07</sup> <sub>-0.10</sub>	0.05 <sup>+0.56</sup> <sub>-0.23</sub>	0.12	-9.92 <sup>+0.63</sup> <sub>-0.30</sub>	9.40 <sup>+0.10</sup> <sub>-0.36</sub>
PTF09fsr	Ib	10.85 <sup>+0.03</sup> <sub>-0.02</sub>	0.27 <sup>+0.03</sup> <sub>-0.02</sub>	0.50	-10.58 <sup>+0.00</sup> <sub>-0.00</sub>	9.60 <sup>+0.01</sup> <sub>-0.08</sub>
PTF09g	II	9.85 <sup>+0.05</sup> <sub>-0.16</sub>	0.17 <sup>+0.02</sup> <sub>-0.02</sub>	0.19	-9.68 <sup>+0.96</sup> <sub>-0.00</sub>	9.30 <sup>+0.04</sup> <sub>-0.61</sub>
PTF09gof	II	10.17 <sup>+0.03</sup> <sub>-0.10</sub>	0.25 <sup>+0.40</sup> <sub>-0.00</sub>	0.35	-9.92 <sup>+0.45</sup> <sub>-0.00</sub>	9.40 <sup>+0.01</sup> <sub>-0.25</sub>
PTF09gtt	II	9.03 <sup>+0.13</sup> <sub>-0.20</sub>	0.18 <sup>+0.43</sup> <sub>-0.73</sub>	0.03	-8.85 <sup>+0.58</sup> <sub>-0.83</sub>	8.80 <sup>+0.51</sup> <sub>-0.55</sub>
PTF09hdo	II	10.80 <sup>+0.07</sup> <sub>-0.14</sub>	0.88 <sup>+0.83</sup> <sub>-0.65</sub>	0.87	-9.92 <sup>+0.94</sup> <sub>-0.66</sub>	9.40 <sup>+0.22</sup> <sub>-0.58</sub>
PTF09hgz	II	10.42 <sup>+0.09</sup> <sub>-0.19</sub>	0.50 <sup>+1.02</sup> <sub>-0.65</sub>	0.51	-9.92 <sup>+1.20</sup> <sub>-0.66</sub>	9.40 <sup>+0.28</sup> <sub>-0.70</sub>
PTF09iex	II	8.00 <sup>+0.21</sup> <sub>-0.41</sub>	-0.27 <sup>+1.67</sup> <sub>-0.53</sub>	-0.48	-8.27 <sup>+1.67</sup> <sub>-0.71</sub>	8.30 <sup>+0.61</sup> <sub>-1.71</sub>
PTF09ige	II	9.83 <sup>+0.04</sup> <sub>-0.09</sub>	0.15 <sup>+0.30</sup> <sub>-0.01</sub>	0.18	-9.68 <sup>+0.55</sup> <sub>-0.00</sub>	9.30 <sup>+0.03</sup> <sub>-0.32</sub>
PTF09igz	II	9.45 <sup>+0.10</sup> <sub>-0.58</sub>	-0.23 <sup>+2.35</sup> <sub>-0.15</sub>	-0.14	-9.68 <sup>+2.88</sup> <sub>-0.24</sub>	9.30 <sup>+0.10</sup> <sub>-2.51</sub>
PTF09ism	II	9.26 <sup>+0.09</sup> <sub>-0.14</sub>	-0.21 <sup>+0.65</sup> <sub>-0.15</sub>	-0.19	-9.47 <sup>+0.75</sup> <sub>-0.21</sub>	9.20 <sup>+0.13</sup> <sub>-0.54</sub>
PTF09ps	Ic	8.86 <sup>+0.54</sup> <sub>-0.11</sub>	2.06 <sup>+0.15</sup> <sub>-2.37</sub>	1.16	-6.80 <sup>+0.10</sup> <sub>-2.88</sub>	6.80 <sup>+2.52</sup> <sub>-0.12</sub>
PTF09q	Ic	10.77 <sup>+0.05</sup> <sub>-0.14</sub>	0.55 <sup>+1.00</sup> <sub>-0.35</sub>	0.67	-10.22 <sup>+1.09</sup> <sub>-0.36</sub>	9.50 <sup>+0.11</sup> <sub>-0.55</sub>
PTF09r	II	9.14 <sup>+0.05</sup> <sub>-0.09</sub>	-1.44 <sup>+0.82</sup> <sub>-0.03</sub>	-1.03	-10.58 <sup>+0.90</sup> <sub>-0.00</sub>	9.60 <sup>+0.05</sup> <sub>-0.30</sub>
PTF09sh	II	10.05 <sup>+0.08</sup> <sub>-0.07</sub>	0.37 <sup>+0.35</sup> <sub>-0.18</sub>	0.37	-9.68 <sup>+0.39</sup> <sub>-0.24</sub>	9.30 <sup>+0.11</sup> <sub>-0.24</sub>
PTF09sk	Ic-BL	8.99 <sup>+0.08</sup> <sub>-0.42</sub>	-0.30 <sup>+2.10</sup> <sub>-0.17</sub>	-0.31	-9.29 <sup>+2.49</sup> <sub>-0.18</sub>	9.10 <sup>+0.17</sup> <sub>-2.31</sub>
PTF09t	II	9.83 <sup>+0.08</sup> <sub>-0.14</sub>	0.36 <sup>+0.64</sup> <sub>-0.15</sub>	0.33	-9.47 <sup>+0.75</sup> <sub>-0.21</sub>	9.20 <sup>+0.11</sup> <sub>-0.54</sub>
PTF09tim	II	10.42 <sup>+0.08</sup> <sub>-0.15</sub>	0.50 <sup>+0.83</sup> <sub>-0.66</sub>	0.52	-9.92 <sup>+0.94</sup> <sub>-0.66</sub>	9.40 <sup>+0.25</sup> <sub>-0.57</sub>
PTF09uj	II	9.79 <sup>+0.08</sup> <sub>-0.05</sub>	0.12 <sup>+0.21</sup> <sub>-0.17</sub>	0.15	-9.68 <sup>+0.21</sup> <sub>-0.24</sub>	9.30 <sup>+0.10</sup> <sub>-0.19</sub>
PTF10bau	II	10.47 <sup>+0.07</sup> <sub>-0.24</sub>	0.79 <sup>+0.99</sup> <sub>-0.25</sub>	0.75	-9.68 <sup>+1.19</sup> <sub>-0.24</sub>	9.30 <sup>+0.16</sup> <sub>-0.82</sub>
PTF10bfz	Ic-BL	8.34 <sup>+0.20</sup> <sub>-0.53</sub>	-0.79 <sup>+3.08</sup> <sub>-0.14</sub>	-0.82	-9.13 <sup>+3.03</sup> <sub>-0.34</sub>	9.00 <sup>+0.21</sup> <sub>-3.00</sub>
PTF10bgl	II	10.61 <sup>+0.07</sup> <sub>-0.11</sub>	0.93 <sup>+0.62</sup> <sub>-0.20</sub>	0.87	-9.68 <sup>+0.70</sup> <sub>-0.24</sub>	9.30 <sup>+0.11</sup> <sub>-0.45</sub>
PTF10bhu	Ic	9.59 <sup>+0.07</sup> <sub>-0.18</sub>	-0.09 <sup>+0.82</sup> <sub>-0.21</sub>	-0.04	-9.68 <sup>+0.96</sup> <sub>-0.24</sub>	9.30 <sup>+0.12</sup> <sub>-0.64</sub>
PTF10bip	Ic	9.01 <sup>+0.13</sup> <sub>-0.08</sub>	-0.12 <sup>+0.24</sup> <sub>-0.69</sub>	-0.23	-9.13 <sup>+0.28</sup> <sub>-0.79</sub>	9.00 <sup>+0.41</sup> <sub>-0.23</sub>
PTF10bzf	Ic-BL	8.23 <sup>+0.25</sup> <sub>-0.07</sub>	1.14 <sup>+0.29</sup> <sub>-0.58</sub>	0.52	-7.09 <sup>+0.20</sup> <sub>-0.77</sub>	7.10 <sup>+0.89</sup> <sub>-0.21</sub>
PTF10cd	II	8.61 <sup>+0.10</sup> <sub>-0.32</sub>	-0.52 <sup>+2.17</sup> <sub>-0.08</sub>	-0.53	-9.13 <sup>+2.43</sup> <sub>-0.16</sub>	9.00 <sup>+0.12</sup> <sub>-2.32</sub>
PTF10con	II	10.29 <sup>+0.07</sup> <sub>-0.49</sub>	0.36 <sup>+1.42</sup> <sub>-0.62</sub>	0.51	-9.92 <sup>+1.86</sup> <sub>-0.66</sub>	9.40 <sup>+0.21</sup> <sub>-1.34</sub>
PTF10cqh	II	10.76 <sup>+0.06</sup> <sub>-0.15</sub>	0.83 <sup>+0.83</sup> <sub>-0.31</sub>	0.84	-9.92 <sup>+0.94</sup> <sub>-0.30</sub>	9.40 <sup>+0.16</sup> <sub>-0.53</sub>
PTF10cwx	II	9.10 <sup>+0.17</sup> <sub>-0.41</sub>	0.61 <sup>+1.59</sup> <sub>-0.83</sub>	0.38	-8.49 <sup>+1.79</sup> <sub>-0.98</sub>	8.50 <sup>+0.70</sup> <sub>-1.83</sub>
PTF10cxq	II	9.10 <sup>+0.09</sup> <sub>-0.12</sub>	-0.18 <sup>+0.56</sup> <sub>-0.11</sub>	-0.20	-9.29 <sup>+0.69</sup> <sub>-0.18</sub>	9.10 <sup>+0.11</sup> <sub>-0.50</sub>
PTF10cxx	II	10.22 <sup>+0.08</sup> <sub>-0.14</sub>	0.30 <sup>+0.82</sup> <sub>-0.66</sub>	0.34	-9.92 <sup>+0.94</sup> <sub>-0.66</sub>	9.40 <sup>+0.22</sup> <sub>-0.53</sub>
PTF10czn	II	10.63 <sup>+0.07</sup> <sub>-0.07</sub>	0.71 <sup>+0.40</sup> <sub>-0.24</sub>	0.71	-9.92 <sup>+0.45</sup> <sub>-0.30</sub>	9.40 <sup>+0.11</sup> <sub>-0.23</sub>

**Table 6** — *Continued*

SN Name	type	M log M <sub>⊙</sub>	SFR (FAST) log M <sub>⊙</sub> /yr	SFR (u) log M <sub>⊙</sub> /yr	SSFR log yr <sup>-1</sup>	Age log yr
PTF10dk	II	8.36 <sup>+0.17</sup> <sub>-0.62</sub>	-1.56 <sup>+2.50</sup> <sub>-0.15</sub>	-1.51	-9.92 <sup>+3.12</sup> <sub>-0.30</sub>	9.40 <sup>+0.12</sup> <sub>-2.60</sub>
PTF10dvb	II	10.13 <sup>+0.11</sup> <sub>-0.20</sub>	0.66 <sup>+0.80</sup> <sub>-0.39</sub>	0.59	-9.47 <sup>+0.98</sup> <sub>-0.45</sub>	9.20 <sup>+0.22</sup> <sub>-0.70</sub>
PTF10hv	II	9.82 <sup>+0.04</sup> <sub>-0.13</sub>	-0.11 <sup>+0.72</sup> <sub>-0.00</sub>	-0.01	-9.92 <sup>+0.79</sup> <sub>-0.00</sub>	9.40 <sup>+0.01</sup> <sub>-0.48</sub>
PTF10in	IIb	8.19 <sup>+0.29</sup> <sub>-0.60</sub>	-0.42 <sup>+1.42</sup> <sub>-1.09</sub>	-0.59	-8.60 <sup>+1.80</sup> <sub>-1.32</sub>	8.60 <sup>+0.83</sup> <sub>-1.88</sub>
PTF10s	II	9.61 <sup>+0.05</sup> <sub>-0.13</sub>	-0.31 <sup>+0.83</sup> <sub>-0.02</sub>	-0.18	-9.92 <sup>+0.94</sup> <sub>-0.00</sub>	9.40 <sup>+0.52</sup> <sub>-0.04</sub>
PTF10ts	II	9.86 <sup>+0.04</sup> <sub>-0.12</sub>	-0.06 <sup>+0.81</sup> <sub>-0.05</sub>	0.04	-9.92 <sup>+0.94</sup> <sub>-0.00</sub>	9.40 <sup>+0.04</sup> <sub>-0.50</sub>
PTF10u	II	9.72 <sup>+0.21</sup> <sub>-0.25</sub>	-3.47 <sup>+2.58</sup> <sub>-0.13</sub>	-0.86	-13.18 <sup>+2.60</sup> <sub>-0.00</sub>	10.00 <sup>+0.00</sup> <sub>-0.46</sub>

**Table 7**  
Cuts to MPA/JHU comparison sample

Criterion	Details	Sample <sup>a</sup>
Within redshift range of sample	0.0189995 < z < 0.103	382095
Successful stellar mass estimate	Mmed > 2 and not INDEF	363881
Successful SFR estimate	SFRavg != -99 and no SFR flag	362395
12+log(O/H) metallicity estimate	OHmed != -99.9	131203
N2 flux ratio in valid range	-2.5 < N2 < -0.3	<b>130370</b>

<sup>a</sup> Remaining sample shown. Cuts are sequential. The sample size of the full MPA/JHU value-added catalog is 927552.